Chapter-V

Rare earth (La^{3+}, Ce^{3+} and Sm^{3+}) doped Sr_2NiMoO_6 as anode system

Paper published and communicated through this chapter

1. ***Pravin Kumar***, *Kumar Singh, Govind Gupta and Prabhakar Singh* Effect of lanthanum (La^{3+}) doping on structural and the electrical properties of double perovskite Sr_2NiMoO_6, RSC Adv., 6 (2016) 22094–22102.*
2. ***Pravin Kumar***, *Nitish Kumar Singh, A.S.K. Sinha and Prabhakar Singh*, Structural and electrical characterizations of cerium (Ce^{3+}) doped double perovskite system Sr_2NiMoO_6, Applied Physics A (2016) 122:828.*
3. ***Pravin Kumar***, *Viviani Massimo and Prabhakar Singh* Effect of samarium (Sm^{3+}) doping on the structural and the electrical conductivity of double perovskite Sr_2NiMoO_6 as anode system for SOFC. (communicated)*

5.1Overview

The double perovskite materials are technologically important due to their great interest for large variety of physical properties (electrical, thermal, magnetic and optical properties) [Huang et al. (2009), Chen et al. (2005) and Ezzahi et al. (2011)]. Double perovskite is a complex system that consists of layered perovskite structure in the form of rock salt-type ordering [Tao et al. (2004) and Taskin et al. (2005)]. It is represented by general formula $A_2B'B''O_6$ where A is an alkaline earth or rare-earth element (A = Sr, Ca, Ba) and B′, B″ are heterovalent transition metals (B′ = Mg, Mn, Fe, Co, Ni, etc. and B″ = Mo, W, Re, Sb, etc.) [Chen et al. (2005) and Vasala et al. (2010)]. It contains two types of octahedral viz BO_6 and $B'O_6$. Although a few materials of double perovskite structure have been investigated for renewable energy techniques [Wilson et al.(2006)]. In renewable energy applications, most of molybdenum based double perovskite materials are promoted for advanced solid oxide fuel cells [Cowin et al. (2011)]. Many of them might play key role in development of electrode materials for SOFC in terms of long-term reliability and advanced ceramic materials [Graves et al. (2010) and Huang et al.(2006)]. In view of their remarkable electrical performance, some specific Mo-based double perovskite ceramics are being appreciated as a potential candidate for anode materials in SOFCs [Ge et al.(2012)]. In view of excellent electrical conductivity, a few double perovskite materials were investigated with substitution of isovalent and aliovalent cations. Influence of doping of isovalent and aliovalent cations at A, B and B′ sites of $ABB'O_6$ have been found to show improved electrical conductivity [Vasala et al. (2010)]. In these materials, Mo based double perovskite ceramics have represented better electrical conductivity in the growth of renewable energy technologies [Huang et al. (2006)]. Recently, some materials of this class such as Sr_2MMoO_6 (M = Mg, Mn, Fe, Co, Ni, Zn etc.) are appreciated due to their high electrical conductivity in different environment (air/H_2/H_2-Ar/CH_4) at lower temperatures [Ge et al. (2012)]. Among them, a few materials play a key role in development of novel anode material due to good compatibility with common electrolyte materials [Cowin et al. (2011) and Ge et al. (2012)]. Therefore, a series of double perovskites materials are studied as a potential candidate for anode materials for SOFC [Sengodan et al. (2014)]. It has already been reported that Ni-doped $Sr_2Fe_{1.5}Mo_{0.5}O_{6-\delta}$ [Xiao et al. (2011 and 2014)], Mn-doped $Sr_2MgMoO_{6-\delta}$ [Li et al. (2011)] and Al-doped Sr_2MgMoO_6 [Xie et al. (2011)] increase the electrical conductivity along with having a good catalytic

activity. A list of trivalent cation (Al^{3+}, La^{3+}, Sm^{3+} etc.) doped Sr_2MgMoO_6 on Sr-site has renovated the electrocatalytic activity and hence, the fuel oxidation and electrochemical performances [Xie et al. (2011), Ji et al. (2007) and Zhang et al. (2010)]. Among them, Vasala et al. [2010] observed that M=Ni represents oxygen stoichiometric and stability under oxidizing condition. Recently, more research groups have also rediscovered doped Sr_2NiMoO_6 for its electrical conductivity and thermal stability [Wei et al. (2008), He et al. (2013) and Filonova et al. (2014)]. Due to its better performance a mixed ionic electronic conductor (MIEC), better stability, good catalytic activity and compability with other cell components, Sr_2NiMoO_6 has been proposed as a suitable anode material for SOFCs [Huang et al. (2009) and Wei et al. (2008)]. Therefore, Sr_2NiMoO_6 system has been optimized for high electrical conductivity, better stability and good thermal matching with LSGM electrolyte [Wei et al. (2008)]. He et al. [2013] reported that Ti substitution in Sr_2NiMoO_6 is responsible for good stability, and appropriate thermal expansion and its compatibility with LSGM electrolyte. The conventional Mo-based double perovskite cermets pass through high temperature sintering process to resolve the presence of impurity phases [Graves et al. (2010)]. It is also reported that some extra phase formation in Mo based double perovskite materials are common, which affects the electrical properties of these materials. The impurities commonly observed in these materials are $SrMoO_4$, Sr_3MoO_6, Ni and NiO [Vasala et al. (2010), He et al. (2013), Vasala et al. (2011) and Xie et al. (2014)].

In this chapter, we have studied the effect of rare earth doping (La^{3+}, Ce^{3+} and Sm^{3+}) doping on structural and electrical properties of double perovskite Sr_2NiMoO_6 system in to three sections Viz. $Sr_{2-x}La_xNiMoO_6$ ($0.02 \leq x \leq 0.10$), $Sr_{2-x}Ce_xNiMoO_6$ ($0.01 \leq x \leq 0.05$) and $Sr_{2-x}Sm_xNiMoO_6$ ($0.01 \leq x \leq 0.05$). These systems have been synthesized by a citrate–nitrate auto combustion method. The structural and electrical properties have been characterized by using XRD (X-ray powder diffraction), TGA/DSC (Thermo gravimetric analysis/Differential scanning calorimetry), SEM (scanning electron microscopy), XPS (X-ray photoelectron spectroscopy) and Impedance spectroscopy, respectively.

5.2 Section-I: Structural and the Electrical Properties of Rare Earth (La^{3+}) Doped Sr_2NiMoO_6 as Anode System

The abbreviations for the system $Sr_{2-x}La_xNiMoO_6$, with x = 0.02, 0.04, 0.06, 0.08 and 0.10 are SLNM02, SLNM04, SLNM06, SLNM08, and SLNM10, respectively. An

appropriate amount of the starting materials having purity more than 99 %, $Sr(NO_3)_2$ (99.9%), $Ni(NO_3)_2 \cdot 6H_2O$ (99%), $(NH_4)_6Mo_7O_{24}.4H_2O$ (99%), La_2O_3 (99.98%) and citric acid were used for preparation of rare earth (La^{3+}) doped SNM system, $Sr_{2-x}La_xNiMoO_{6-\delta}$ (x = 0.02, 0.04, 0.06, 0.08 and 0.10) via citrate-nitrate auto-combustion route. The prepared samples were characterized by XRD, DSC/TG, SEM, XPS and electrochemical impedance technique.

5.2.1 Results and Discussion

5.2.1.1 Powder X-ray Diffraction (XRD)

Figure 5.1 shows the XRD pattern of the powder samples of the system $Sr_{2-x}La_xNiMoO_{6-\delta}$ (x = 0.02, 0.04, 0.06, 0.08 and 0.10). These patterns show the formation of well crystallized nature of the samples.

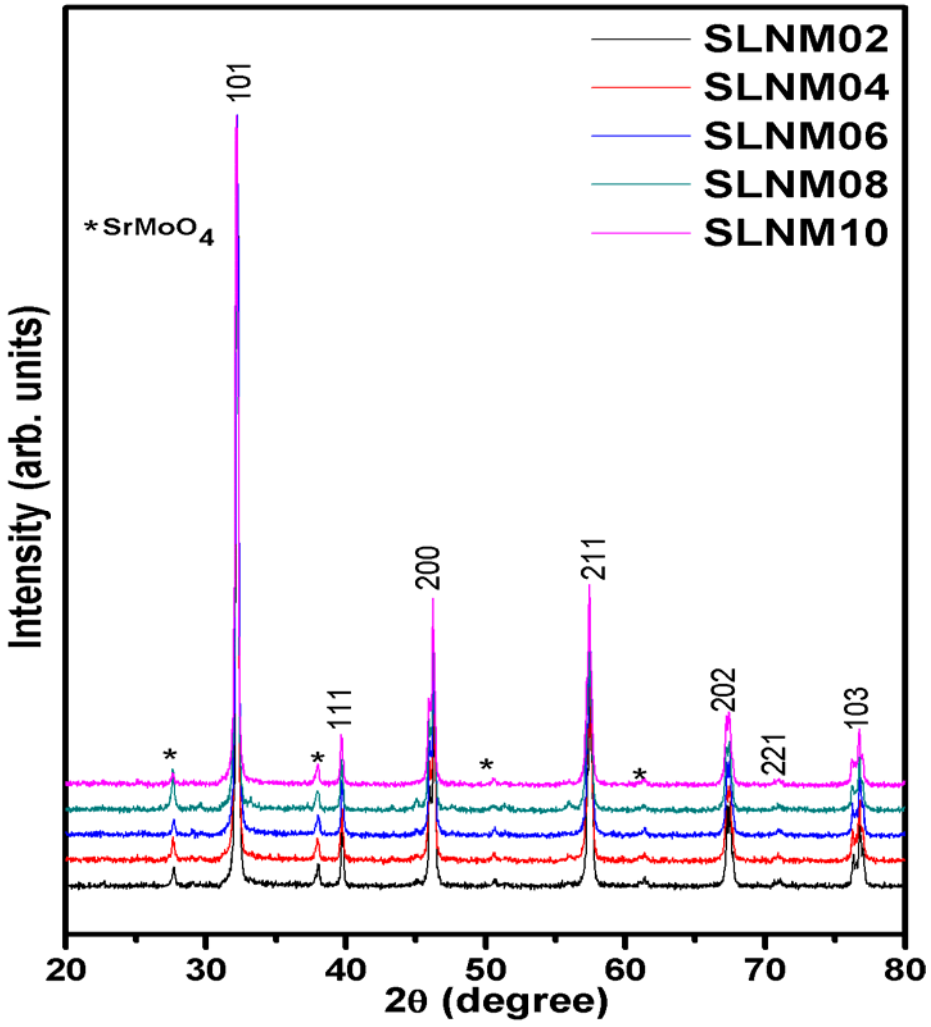

Fig.5.1 *The X-ray diffraction pattern of different samples: SLNM02, SLNM04, SLNM06, SLNM08 and SLNM10. Asterisk (*) indicates the $SrMoO_4$ phase.*

The peaks corresponding to major phase could be indexed on the basis of double perovskite tetragonal phase Sr_2NiMoO_6 with space group *I4/m* using JCPDS card no. 15-0601. All the samples of the system SLNM-x show the peak corresponding to a minor phase at ~27.67°. This phase was identified as scheelite type $SrMoO_4$ with the help of standard JCPDS card no. 85-0586. The determined average crystallite size and experimental density of each composition was observed from Archimedes Principle and are shown in Table 5.1. Also, Figure 5.2(a)-(e) shows the Rietveld refinement of XRD data of the system SLNM-x using Fullprof software. In the Rietveld refinement, the peak profile was refined by the Thompson-Cox In this refinement, Yobs, Ycal, and Yobs-Ycal represent the experimental data, calculated data, and the difference of experimental and calculated data, in that order.

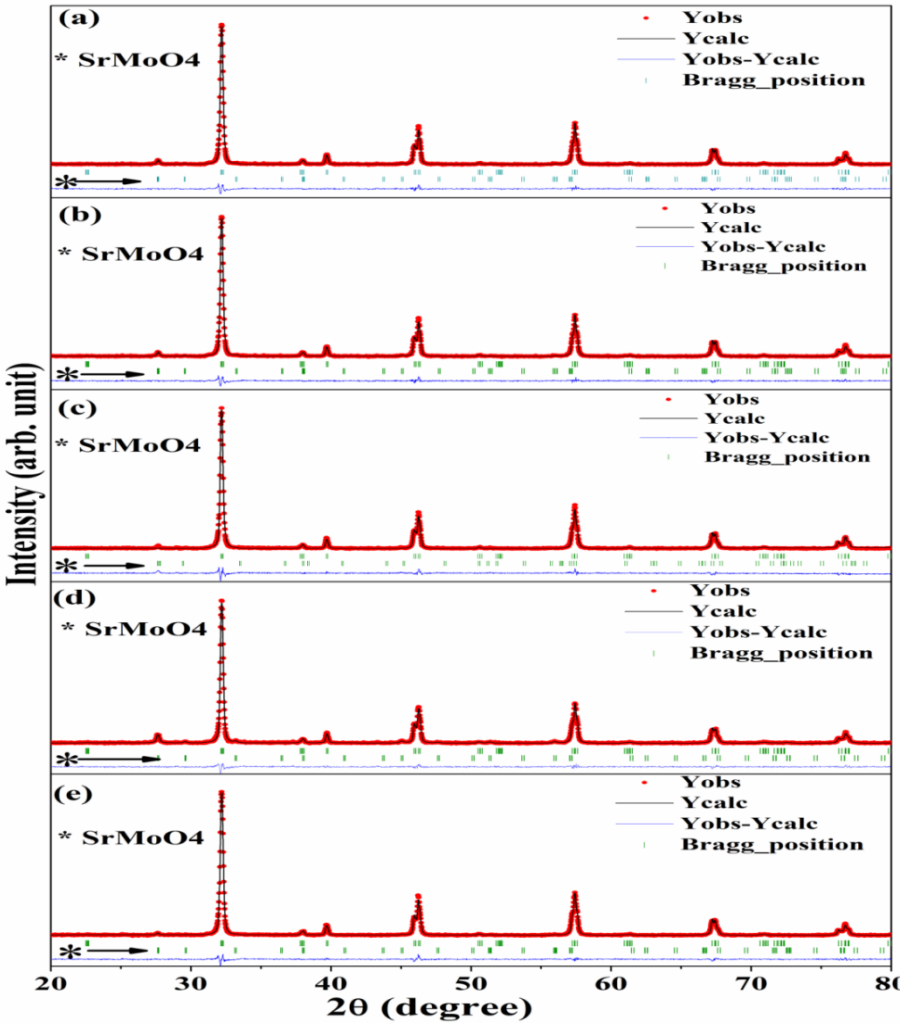

Fig.5.2. *Reitveld refinement of X-ray diffraction pattern of different samples (a) SLNM02, (b) SLNM04, (c) SLNM06, (d) SLNM08 and (e) SLNM10.*

Hastings pseudo-Voigt functions while the background was refined with six coefficients polynomial function. The Rietveld refinement also confirms the presence of SrMoO4 phase (indicated with asterisk symbol). The Refined parameters are also given in Table5.1. From this table, one can observe that the cell parameters for all the compositions are almost constant except the composition SLNM04 for which it is minimum. The average crystallite size and lattice strain for all powder samples was also determined. We also observe that for x = 0.04 composition the volume fraction of the SrMoO4 phase is maximum and it has the lowest lattice strain. However, considering the doping of La^{3+} ion, which has smaller ionic radii (1.03 Å) compared to that of Sr^{2+} (1.18 Å), it is expected that the lattice parameter should decrease with the increase of dopant's concentration. In present case, no such trend is observed. It appears that the lattice strain and the impure phase together govern the structural behaviour of the system. The increase in the lattice constant due to La3+ doping is compensated by the lattice strain and impure phase [Ma et al. (2014)].

Table5.1. *Variation in lattice parameters of SLNM-x (x = 0.02, 0.04, 0.06, 0.08 and 0.10) system.*

Table 5.1									
Samples	Lattice Parameters			Crystall-ite Size (nm)	Experi-mental density (g/cm^3)	% porosity	χ^2	% of volume fraction of $SrMoO_4$	Average Lattice Strain ($\times 10^{-4}$)
	a (Å)	b = c (Å)	Cell Volume $(Å)^3$						
SLNM02	5.549	7.897	243.220	59.78	5.7	50.35	2.66	3.45	10.35
SLNM04	5.539	7.882	241.803	52.33	5.8	49.52	4.18	14.31	6.13
SLNM06	5.553	7.902	243.629	58.92	5.8	49.70	2.71	4.86	12.13
SLNM08	5.548	7.896	243.039	72.13	5.7	50.61	3.06	9.53	11.99
SLNM10	5.555	7.906	243.962	65.87	5.7	50.95	6.66	8.76	10.19

5.2.1.2 Thermal Analysis

The thermal analysis of sintered samples is studied through DSC/TGA. Figure.5.3 shows the DSC/TG curve of sample SLNM04 in N_2 atmosphere and temperature range from RT to 1000 °C. The TG curve shows three steps weight losses at around 100, 300 and 750 °C. In DSC curve, three endothermic peaks were observed corresponding to above three weight loss in TG curve. The first weight loss at ~100 °C can be ascribed to loss of moisture in the sample. The second weight loss at ~300 ºC may be attributed to loss of lattice oxygen while the third weight loss at a temperature higher than 500 °C may be assigned to formation of more oxygen vacancies accompanied with reduction of Mo^{6+} in to Mo^{5+} [Jiang et al. (2014) and Logvinovich et al. (2008)]. A similar behaviour was also observed for the other samples. The reduction of Mo^{6+} in Mo^{5+} is also confirmed in our XPS studies that are discussed in the forthcoming part.

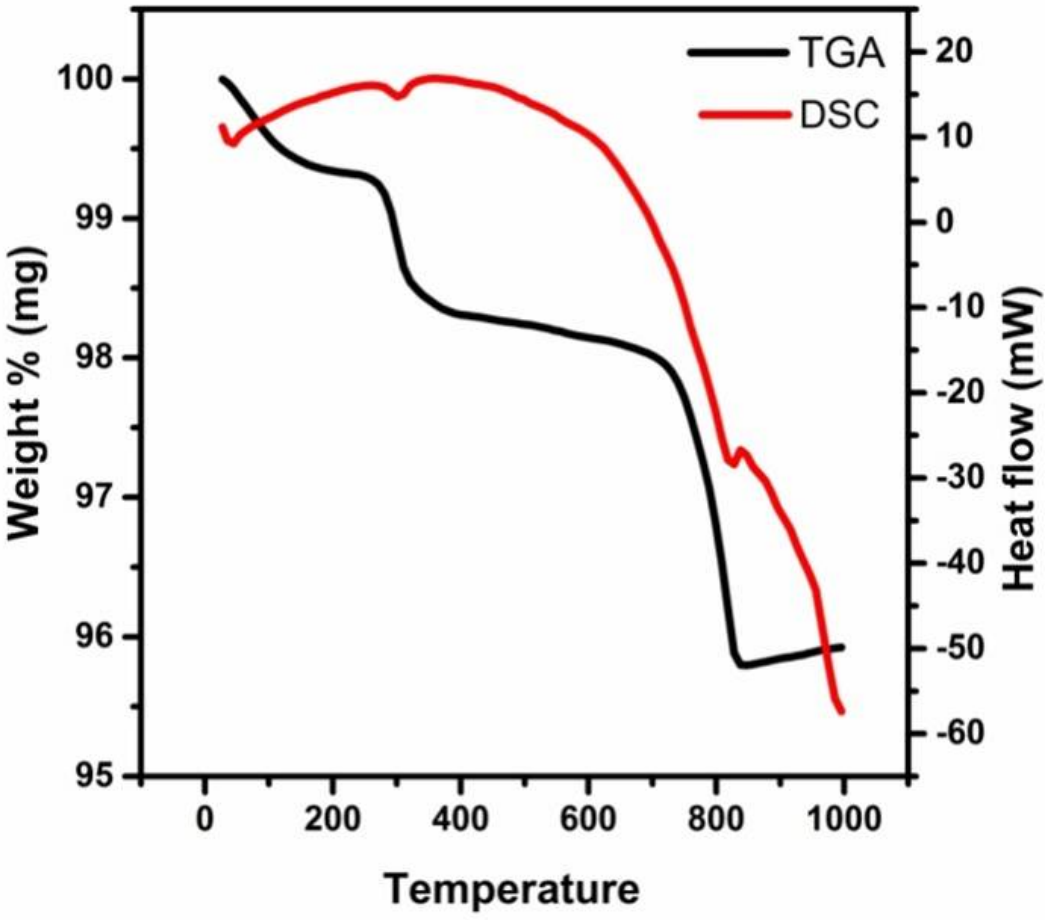

Fig.5.3 *DSC/TG curve for sintered SLNM04 in N_2 atmosphere from RT to 1000 °C.*

5.2.1.3 Surface Morphology

The surface morphologies of the samples have been studied using FESEM after chemically etching. Figure 5.4(a)–(e) shows FESEM images of chemically etched samples sintered at 1350 °C. A look on the FESEM image reflects that all the samples are composed of the fine grains of irregular shape and size. It also reflects that all the samples have some porosity as mentioned in Table5.1. The average grain size of compositions SLNM02, SLNM04, SLNM06, SLNM08 and SLNM10 calculated by linear intercept method is found to be approximately ~1.59 µm, ~1.52 µm, ~1.75 µm, ~1.42 µm and ~1.26 µm, respectively. Initially, up to x= 0.06 the grain size is almost constant and thereafter a slight decrease in the grain size is observed. For higher substitutions i.e x > 0.06, the La^{3+} ions segregate at the grain boundaries due to the charge difference and ionic size difference between the La^{3+} and Sr^{2+} ions. This segregation further inhibits the grain growth and results a decrease in the grain size [Desu et al.(1990) and Dwivedi et al. (2007)].

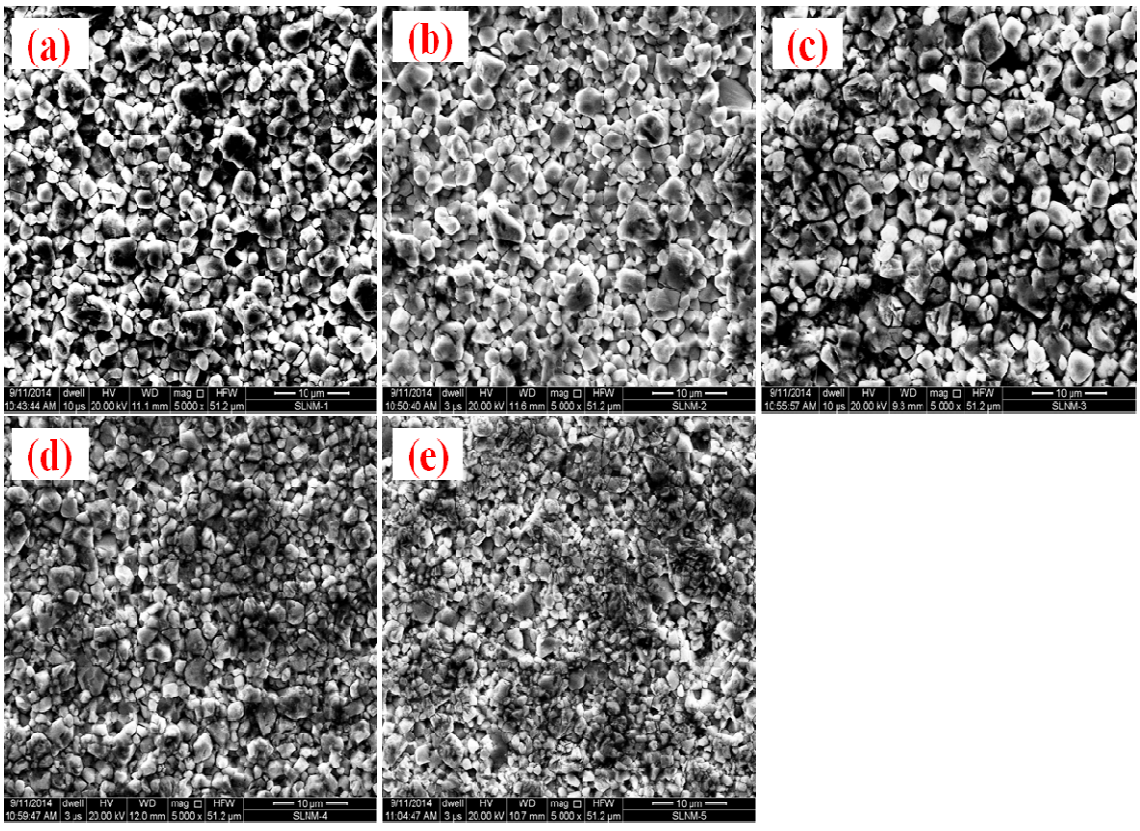

Fig.5.4. *Field emission scanning electron micrograph of chemically etched various compositions (a) SLNM02, (b) SLNM04, (c) SLNM06, (d) SLNM08 and (e) SLNM10.*

5.2.1.4 XPS Analysis

To detect the type of charge carriers present in the system SLNM-x, XPS analysis has been done. The XPS spectra corresponding to Mo and O in the system SLNM-x are schematically shown in Fig.5.5 (a)-(b). The XPS spectra were corrected with respect to C-1s peak appeared at ~284.6eV.

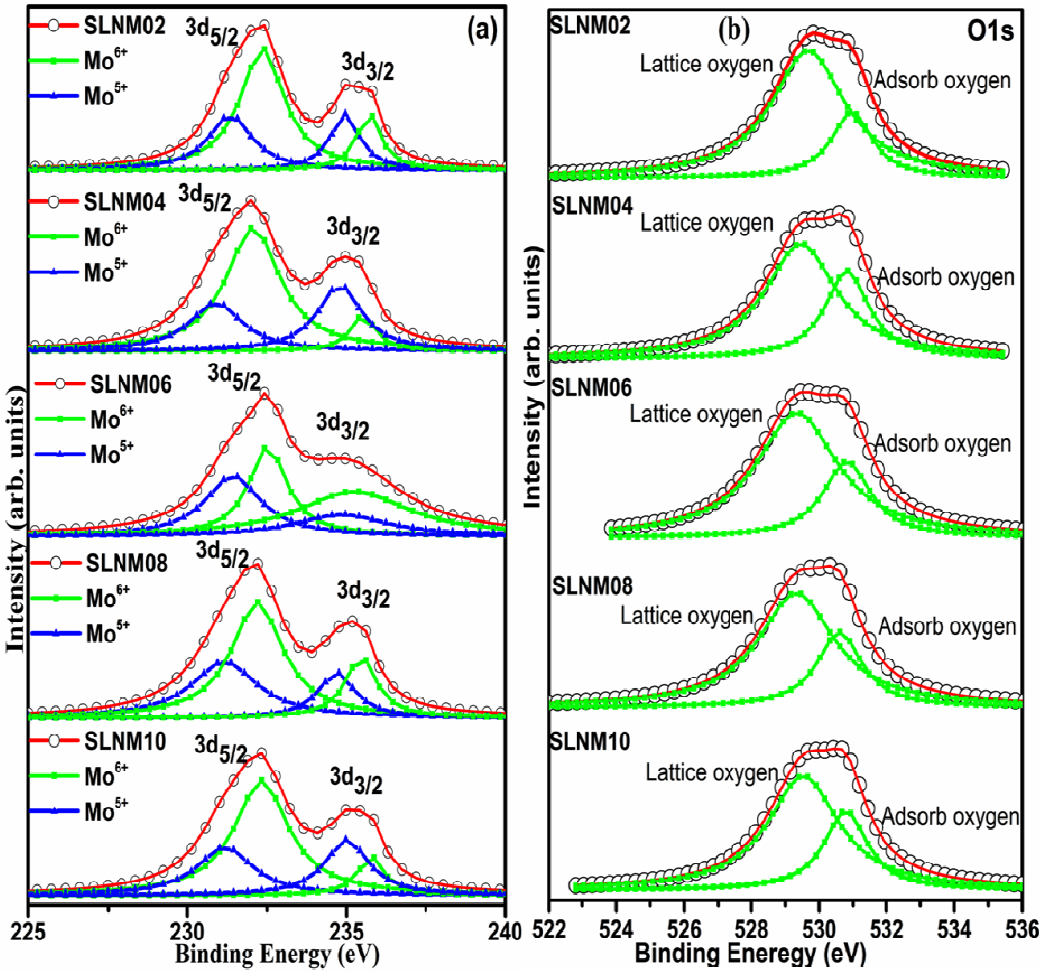

Fig.5.5. *XPS spectra for compositions SLNM02, SLNM04, SLNM06, SLNM08 and SLNM10:* ***(a)*** *Mo-3d, and* ***(b)*** *O-1s.*

Figure 5.5 (a) reveals the Mo-3d core level spectra which are splitted into two asymmetrical peaks for all the samples. These peaks could be assigned to $3d_{5/2}$ and $3d_{3/2}$ state of Mo. These two asymmetrical peaks could be fitted into two pairs of peaks. These fitted two pairs of peaks correspond to Mo^{5+} and Mo^{6+} states, respectively [Dambies et al. (2001)]. This indicates the coexistence of mixed valance state of Mo^{5+}/Mo^{6+} for all samples. It is observed that La^{3+} substitution on Sr^{2+} site varied the ratio of Mo^{5+}/Mo^{6+} which was determined by the ratio of

the integrated area of the peaks corresponding to Mo^{6+} and Mo^{5+} states. The brief descriptions about each peak for all the samples are given in Table 5.2. The sample SLNM04 has highest value of ratio Mo^{5+}/Mo^{6+} as compared to other samples. In these spectra are broader and asymmetrical in nature for all the compositions. Hence, the peak for all the samples could be splitted into two peaks and attributed to two different types of oxygen species: lattice oxygen and adsorbed oxygen. The percentage of adsorbed oxygen for all the samples is given in Table5.2. Sample SLNM04 has highest percentage of adsorbed oxygen as compared to other samples. Thus the composition SLNM04 will show better catalytic activity towards the oxygen association/dissociation process [Ge et al. (2012)].

Table5.2. *The XPS fitting results of Mo-3d spectra and percentage of adsorbed oxygen of the system SLNM-x ($0.02 \leq x \leq 0.10$).*

Table5.2							
Compositions	Parameters	Mo^{6+}		Mo^{5+}		Mo^{5+}/Mo^{6+}	Adsorbed oxygen %
		$3d_{5/2}$	$3d_{3/2}$	$3d_{5/2}$	$3d_{3/2}$		
SLNM02	Binding Energy(eV)	232.39	235.82	231.40	234.98	0.59	22.24
	Area	6206.23	1561.42	2742.49	1866.49		
SLNM04	Binding Energy(eV)	231.99	235.43	230.91	234.78	0.71	31.78
	Area	4972.60	648.29	1885.44	2142.79		
SLNM06	Binding Energy(eV)	232.39	235.43	231.50	235.08	0.63	26.26
	Area	3101.15	4529.71	3026.51	1829.29		
SLNM08	Binding Energy(eV)	232.26	235.62	231.24	234.78	0.68	27.62
	Area	4756.73	1507.74	2943.58	1308.85		
SLNM10	Binding Energy(eV)	232.29	235.88	231.25	234.98	0.69	29.64
	Area	4843.54	788.14	2060.20	1838.64		

5.2.1.5 Impedance Spectroscopy

Impedance Spectroscopy (IS) is an effective and simple tool to study the electrical properties of the polycrystalline materials. It facilitates the tailoring of polycrystalline materials by separating out the contribution of different parts i.e. grain, grain-boundary and electrode-specimen interface to the electrical conductivity [Boukamp (2004) and Jamnik (2003)]. Thus, this tool is applied to analyze the effect of La doping on the electrical property of Sr_2NiMoO_6. To study the evolution of impedance with temperature, the complex plane impedance plots were drawn at different temperatures for all samples. As a representative, among these plots a few plots for sample SLNM04 with nonlinear curve fitting are shown in Fig.5.6(a)-(f).

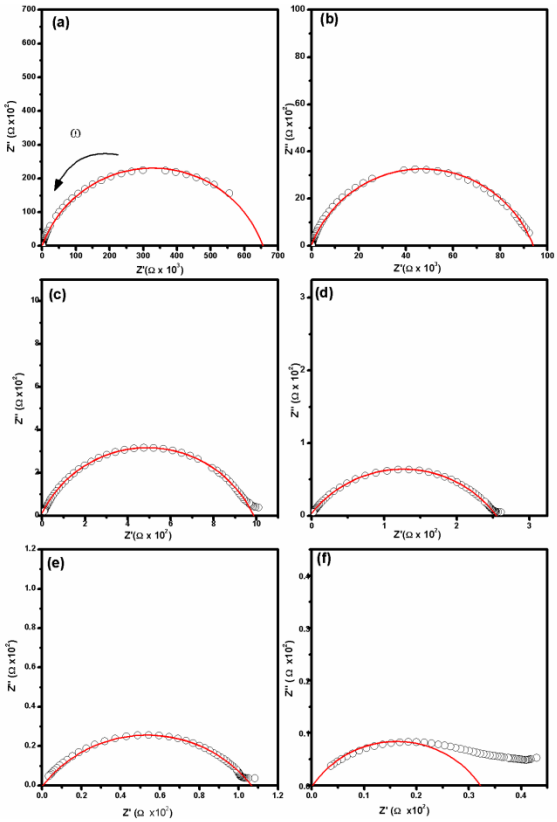

Fig. 5.6. *The complex plane Impedance plots for the composition SLNM04:* ***(a)*** *200 °C,* ***(b)*** *275 °C,* ***(c)*** *350 °C,* ***(d)*** *475 °C,* ***(e)*** *525 °C and* ***(f)*** *600 °C.*

From the above figure one can observe that a part of one depressed semicircular arc appears at 200 °C which grew with increase of temperature with tendency to complete this arc. With further increase in temperature, again a part of depressed semicircular arc with a tail at one end was appeared. The reason behind this nature of impedance spectra is decrease in

relaxation time of different contributions with increase in temperature. The capacitance corresponding to observed semicircular arc was calculated by the relation $2\pi fRC=1$, where f, R and C are peak frequency, resistance and capacitance, respectively, which holds good at the peak of the corresponding semicircular arc. The capacitance found to be in order of the nF. Primarily, it indicates that the observed semicircular arc represents the contribution of grain-boundaries. But, there may be another possibility that the observed semicircular arc is due to combined contribution of grains and grain-boundaries. Thus, to confirm whether this is due to only grain-boundaries or grains and grain-boundaries both, the analysis of data by modulus spectroscopy is also needed. The modulus plots for the sample NM04 at different temperatures are shown in Fig. 5.7 (a)-(d).

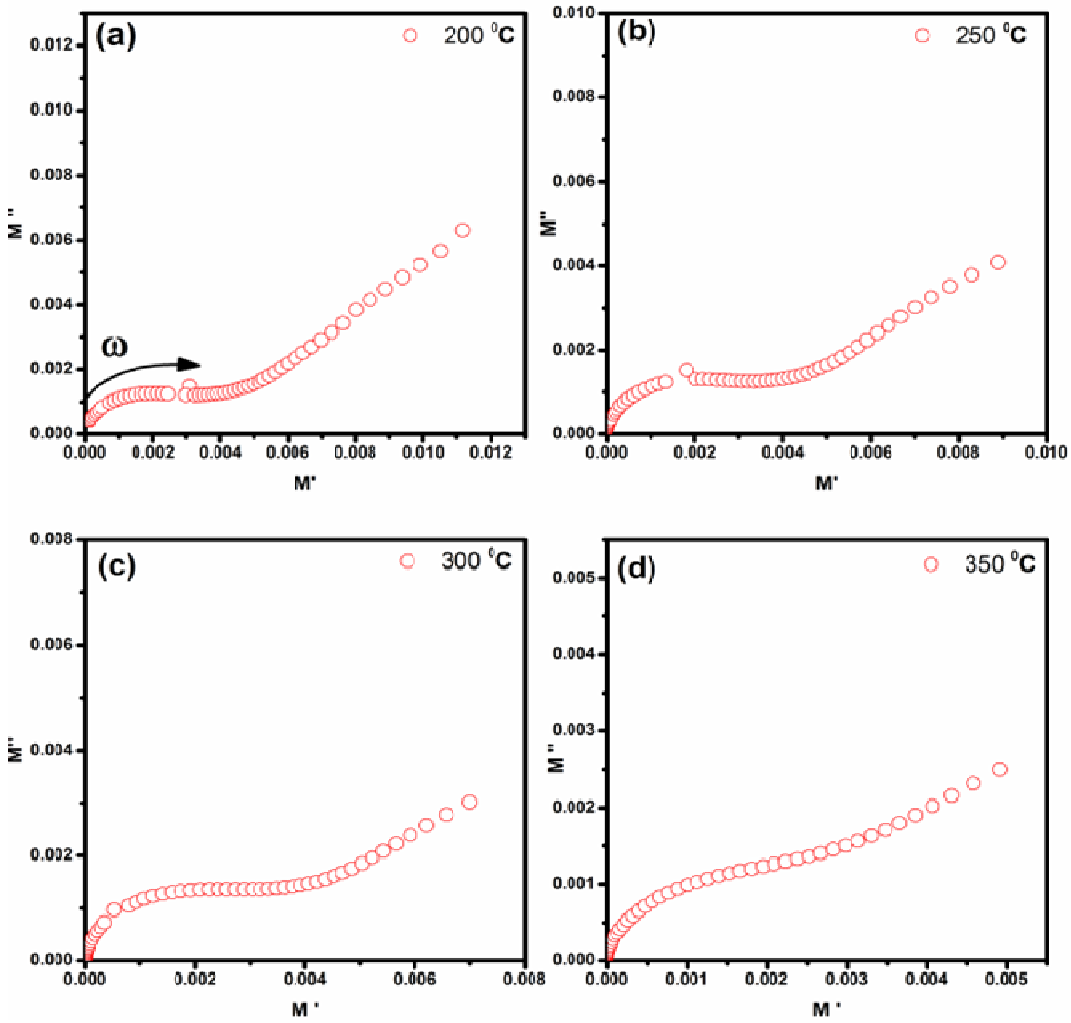

Fig. 5.7. *The modulus spectra for the composition SLNM04 at:* ***(a)*** *200 °C,* ***(b)*** *250 °C,* ***(c)*** *300 °C and* ***(d)*** *350 °C.*

In these plots, a part of depressed semicircular arc with a tail at one end was also observed. The capacitance corresponding to observed depressed semicircular arc was also calculated by the relation $2\pi fRC=1$, which holds good at the peak of the corresponding depressed semicircular arc. The capacitance is found to be order of pF. Primarily, it indicates that the observed semicircular arc represents the contribution of grains. But, in the impedance and modulus plots the observed semicircular arc passes through origin. This indicates that the observed depressed semicircular arc in impedance plots should correspond to grains while the calculated capacitance indicates towards the grain-boundaries. In the same manner, in modulus plots, the observed depressed semicircular arc should correspond to grain-boundaries while the calculated capacitance indicates the grains contribution. From above discussions, it can be concluded that in both the plots, observed depressed semicircular arc are same and have contributions from grains as well as from grain-boundaries. The observed difference in capacitances of both the plots is due to dominance of most resistive part i.e. grain-boundaries in impedance and least capacitive part i.e. grains in modulus. Here the separation of grains and grain-boundaries contributions is not observed, because of the comparable relaxation times of both the contributions.

To show the variation of impedance for all compositions, typical complex plane impedance plots with nonlinear curve fitting are shown in Fig.5.8 (a)-(f) at 375 °C. Where, Figure 5.8 (a)-(e) represent separate plots for each composition at 375 °C and Figure 5.8 (f) represents the combined plots for all compositions. The above figure clearly indicates that the sample SLNM04 has the lowest impedance. Here, the total resistance, R_t corresponding to both contributions can be obtained from the intercept of the depressed semicircular arc on the real axis while the total conductivity of the samples can be calculated applying the formula

$$\sigma_t = \frac{1}{R_t} \times \frac{L}{S} \qquad (5.1)$$

where σ_t is the total electrical conductivity, L is the thickness of pellet, R_t is the total resistance, and S is the surface area of the pellet. The activation energy of conduction for all the compositions was calculated from the slope of the plot $\log\sigma T$ vs. 1000/T (Fig.5.9) applying the Arrhenius relationship

$$\sigma = \frac{\sigma_o}{T} e^{-\frac{E_a}{kT}} \qquad (5.2)$$

where, σ_0 is known as pre-exponential factor having dependency mainly upon mobile charge carrier density, E_a is the activation energy of conduction, k is the Boltzmann constant and T is the absolute temperature.

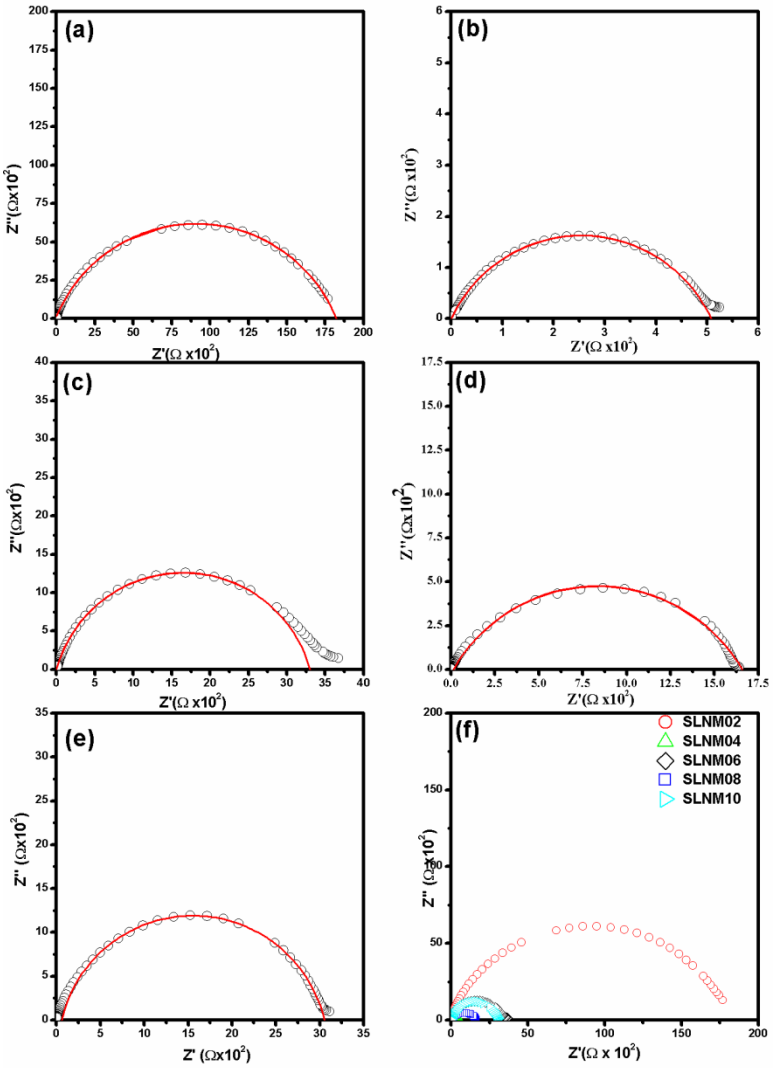

Fig. 5.8. *The complex plane Impedance plots for compositions:* ***(a)*** *SLNM02,* ***(b)*** *SLNM04,* ***(c)*** *SLNM06* ***(d)*** *SLNM08,* ***(e)*** *SLNM10 and* ***(f)*** *combined plot for SLNM-x (0.02 ≤ x ≤ 0.10): at 375 °C.*

The sample SLNM04 possess as higher conductivity than the other samples. The calculated value of activation energy E_a for all the compositions is given in Table5.3. The variation of activation energy E_a and pre-exponential factor σ_0 with compositions are shown in Fig.5.10. The change in electrical conductivity with La^{3+} doping on Sr^{2+} site may be explained by defect chemistry. La^{3+} doping on Sr^{2+} site in SLNM-x ($0.02 \leq x \leq 0.10$) samples creates

electronic charge according to following defect equations. The released electrons enhances the electronic conductivity to the total conductivity

$$La_2O_3 \xrightarrow{SrO} 2La^{\bullet}_{Sr} + 2e' + 2O^{\times}_{O} + \frac{1}{2}O_2 \quad (5.3)$$

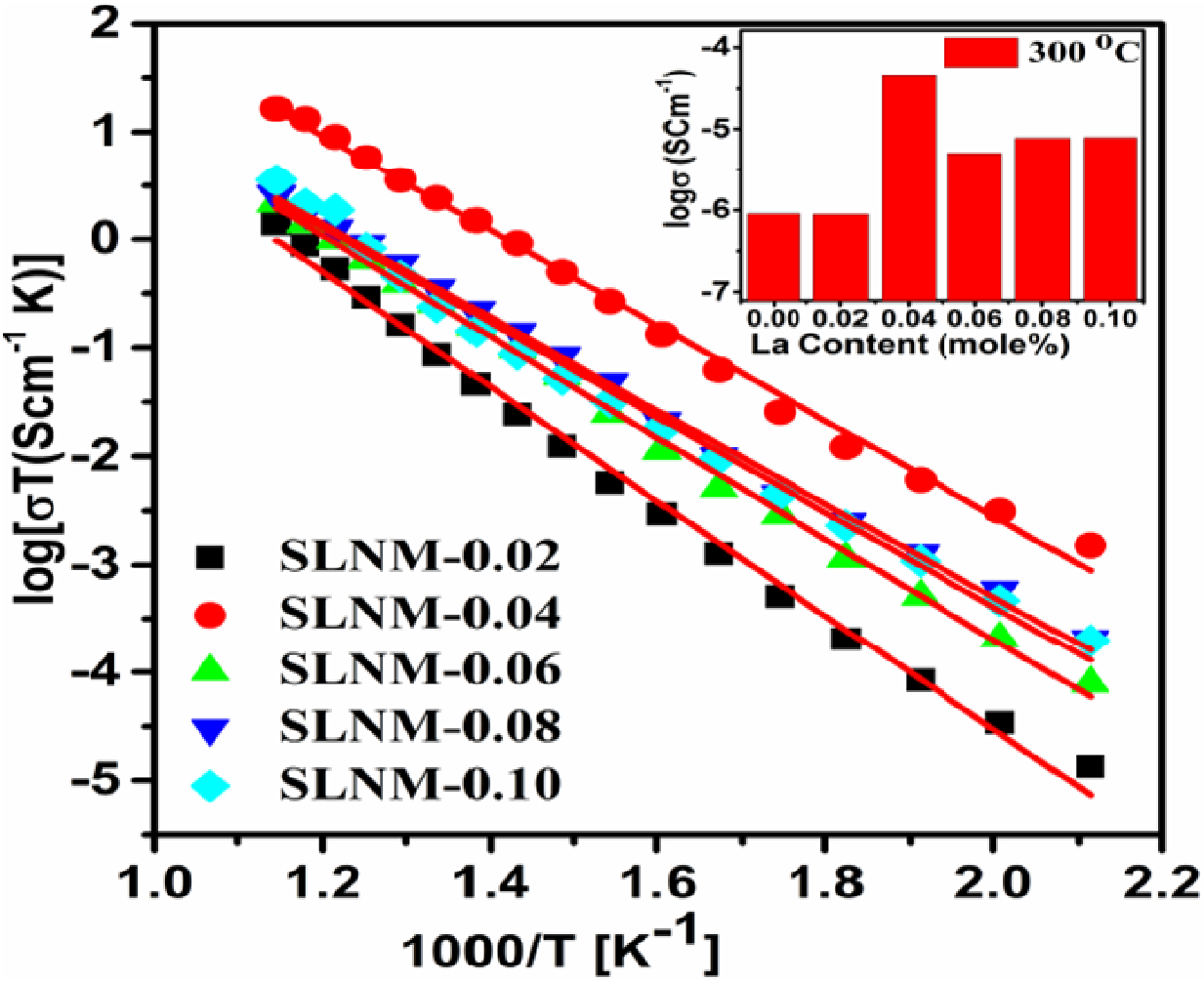

Fig.5.9. *Arrhenius logσ$_t$T vs. 1000/T plots of various samples of the system SLNM-x (0.02 ≤ x ≤ 0.10). The inset depicts the variation of logarithms of conductivity with composition at 300 °C.*

The former will increase the electronic conductivity while the latter will decrease the oxide ion conductivity. From the Table 5.3 it is clear that the value of activation energy E_a for the samples SLNM04, SLNM06, SLNM08 and SLNM010 is lower than the sample SLNM02 due to easy hopping of electronic charge between Mo^{6+} and Mo^{5+} and also, the low contribution of oxide ion conduction [Dorai et al. (2013)]. But on further doping there is no

appreciable change in activation energy of the samples. Relative to SLNM02, all the other samples have high value of conductivity. Sample SLNM04 shows the highest value of conductivity.

Table.5.3. Activation energy of SLNM-x (x= 0.02, 0.04, 0.06, 0.08 and 0.10) system.

Compositions	Activation energy, E_a (eV)	Pre-exponential factor σ_0
SLNM02	$E_a = 1.1$	1.11×10^6
SLNM04	$E_a = 0.84$	1.72×10^6
SLNM06	$E_a = 0.91$	4.25×10^5
SLNM08	$E_a = 0.86$	2×10^5
SLNM10	$E_a = 0.87$	2.2×10^5

Huang et al. [2009] have reported that in Sr_2MMoO_6 (M = Co, Ni) system, $SrMoO_4$ may block the catalytic pathways for reforming the fuels and thus its presence is not desirable for SOFC application. In their work, the formation of $SrMoO_4$ was taken place after exposure to CH_4. But in our system, $SrMoO_4$ is already present along with main phase of Sr_2NiMoO_6. Kubo et al. [2004] has reported that this phase has catalytic activity for hydrocarbon oxidation, which could be advantageous in SOFC anode use. Also Vasala et al. [2011] reported that under reducing atmosphere the $SrMoO_4$ is reduced to $SrMoO_3$, which actually increases the electrical conductivity. However, in the present case conductivity measurement was done in air. Yuan at al.[2004] has mentioned that presence of $SrMoO_4$ phase can alter the physical properties of the system. Thus increase and/or decrease of conductivity of the system will also depend on the volume fraction of this additional phase. Therefore, in the present case, the role of $SrMoO_4$ phase in the $Sr_{2-x}La_xNiMoO_6$ cannot be denied. From the Rietveld analysis (Table.5.1) it is clear that for the system SLNM04 having the maximum impurity shows the highest conductivity. Further, the lattice strain analysis (Table.5.1) indicates that SLNM04 bears the minimum lattice strain, and all other samples show almost double lattice strain in comparison to this composition. The low lattice strain may cause less charge polarization leading to high value of conductivity in the system SLNM04 [Wen et al. 2015].

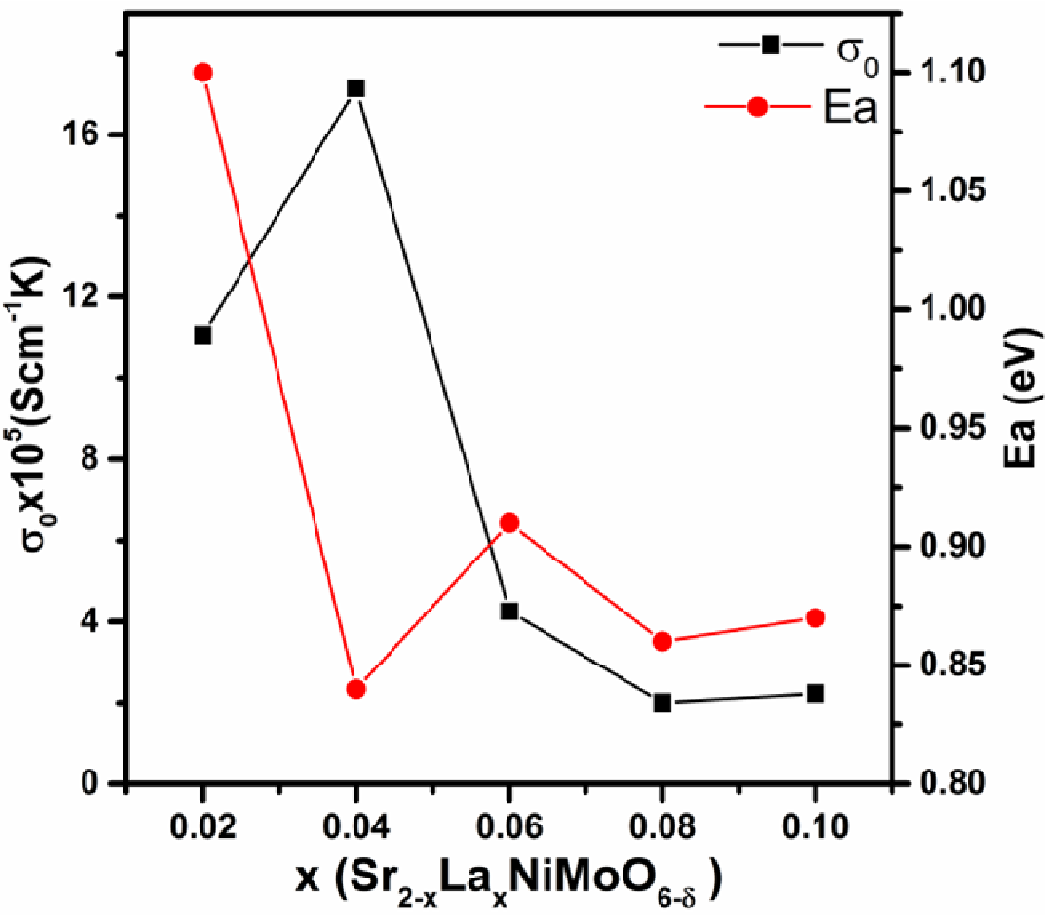

Fig.5.10 *Variation of pre-exponential factor σ_0 and activation energy with respect to doping concentration x of the system SLNM-x ($0.02 \leq x$ 0.10).*

The other reason behind this highest conductivity in SLNM04 could also be due to enhancement of electronic charges (Mo'_{Mo}) as per equation 5.4. The XPS data showing the ratio of $M0^{5+}$ and Mo^{6+} (Table.5.2) also supports the reduction process as mentioned in equation5.4. The XPS data indicates that the ratio of Mo^{5+}/Mo^{6+} is highest for SLNM04 due to more oxygen vacancies corresponding to high percentage of adsorbed oxygen as compared to other samples. The variation of percentage of adsorbed oxygen in XPS data corroborate with the variation of the Mo^{5+}/Mo^{6+} ratio (Table.5.2). At the same time, the decrease in conductivity on doping higher than 4% may be due to formation of associate pairs between Mo'_{Mo} and $V_o^{\bullet\bullet}$ [Xie et al. (2011)]. Also it can be seen from Table.5.3 that with increasing concentration of La^{3+}, pre-exponential factor σ_0 (i.e. mobile charge carriers) increases up to 4% thereafter shows a decreasing trend and slight increase for 10% doping. But the activation energy decreases with the increasing pre-exponential factor σ_0 up to 4% and shows a

decreasing trend with decrease in pre-exponential factor σ_0. The decrease in pre-exponential factor σ_0 at higher doping may be due to the formation of associate pairs between Mo'_{Mo} and $V_o^{\bullet\bullet}$ which increases the activation energy and lowers the effective number of charge carriers contributing to the conduction process. The variation of σ_0 with composition supports the formation of associate pairs at higher doping, which act as a lowering factor for the conductivity as discussed above. Figure5.9 clearly reveals that the composition $Sr_{1.96}La_{0.04}NiMoO_6$ (SLNM04) shows the maximum conductivity. Hence, it was considered worthwhile to measure the electrical conductivity for this composition in reducing atmosphere.

5.2.1.6 Conductivity measurement of La^{3+} doped Sr_2NiMoO_6 in Reducing Atmosphere

Figure5.11 shows the plots of resistance as function of temperature for La^{3+} doped Sr_2NiMoO_6 (SLNM04) system in reduced H_2 atmosphere, which was measured in temperature range of 100-700 °C during the cooling cycle.

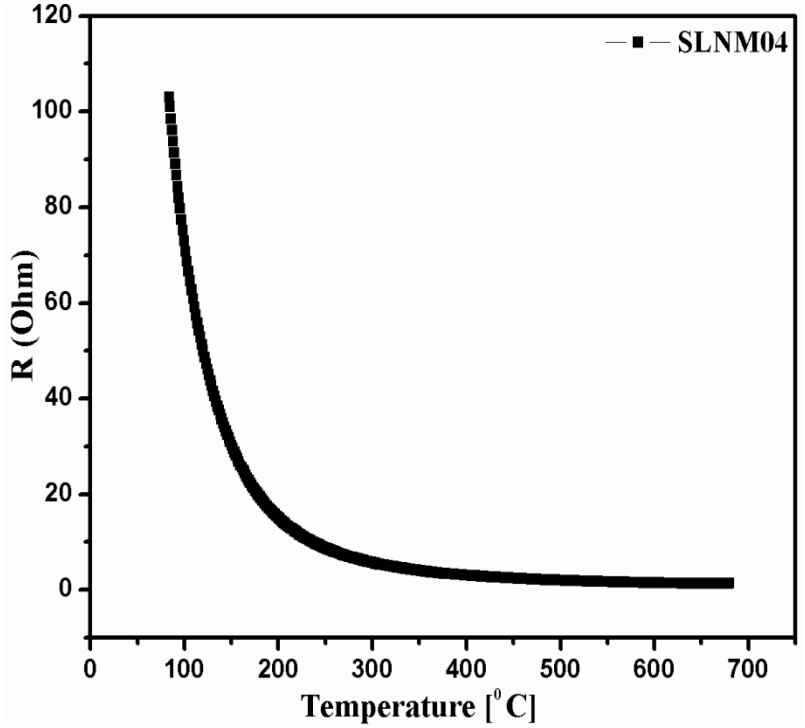

Fig.5.11 *The plots of Resistances (R) vs. Temperature for the $Sr_{1.96}La_{0.04}NiMoO_{6-\delta}$ (SLNM04) sample in H_2 atmosphere.*

This figure clearly reveals that resistance value decreases with increasing of temperature and get almost constant above 500 ^{0}C. Figure 5.12 shows the Arrhenius plots of electrical

conductivity (σ) of sample (SLNM04) was measured in H_2 and air in the temperature range of 300-600 °C. Figure5.12. clearly reveals that conductivity increases with applying reducing atmosphere of H_2. The highest electrical conductivity for SLNM04 was obtained with a value of 1.8 Scm^{-1} at 909 K in H_2. The activation energy (Ea) for electron transportation was calculated by Arrhenius plot of the electrical conductivity was found 0.29 eV and 0.93 eV in H_2 and air respectively. The increase in electrical conductivity in reducing atmosphere (H_2) having a system in which a higher valent dopant substitutes a lower valent dopant (donor doping) can be understood using defect equations [Xie et al. (2011) and Doari et al. (2013)].

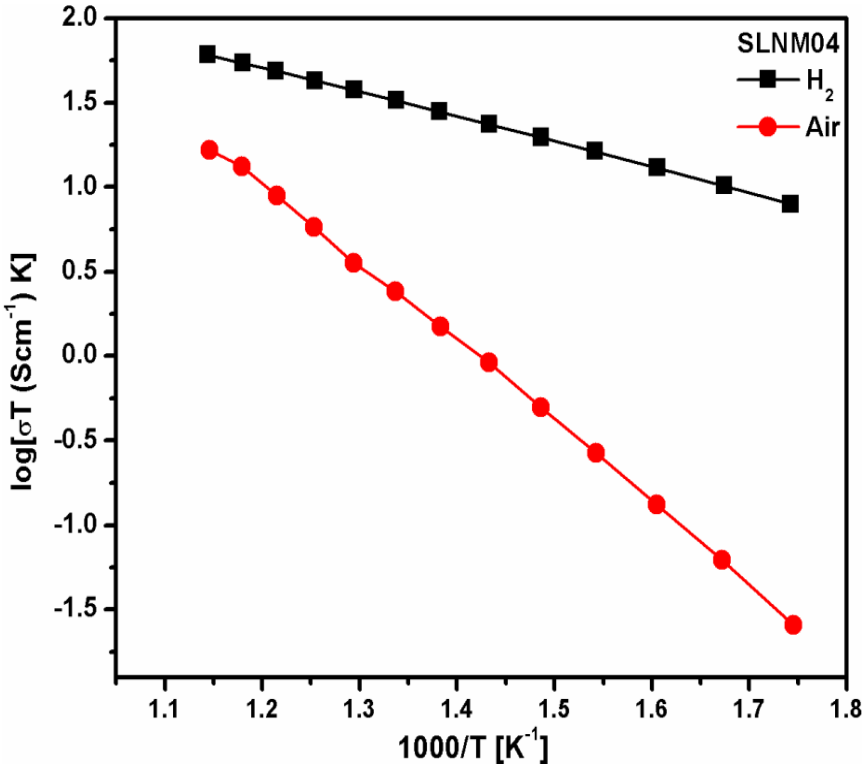

Fig.5.12. *Arrhenius plots of conductivity for the $Sr_{1.96}La_{0.04}NiMoO_{6-\delta}$ (SLNM04) sample in H_2 and air atmosphere.*

La^{3+} substituted on Sr^{2+} site in Sr_2NiMoO_6 system can be studied from the following defect eqns.

$$\left.\begin{aligned} La_2O_3 \xrightarrow{SrO} 2La_{Sr}^{\bullet} + 2e' + 2O_O^{\times} + \tfrac{1}{2}O_2 \uparrow \\ Mo_{Mo}^{\times} + e' \rightarrow Mo_{Mo}' \end{aligned}\right\} \qquad (5.6)$$

where deficiency of lattice oxygen may be created in the presence of reducing atmosphere (H_2), generating the oxygen vacancies and reduction of Mo^{6+} to Mo^{5+} ions for the electrovalent charge compensation can be explained by the following defect Eq^n.

$$2\mathrm{Mo}_{\mathrm{Mo}}^{\times} + \mathrm{O}_{\mathrm{O}}^{\times} \rightarrow 2\mathrm{Mo}'_{\mathrm{Mo}} + \mathrm{V}_{\mathrm{o}}^{\bullet\bullet} + \frac{1}{2}O_2(g) \uparrow \quad (5.7)$$

where electronic charge $\mathrm{Mo}'_{\mathrm{Mo}}$ may confirm Mo^{5+} substitution on Mo^{6+} site. The electro-neutrality mechanism can be described by following defect Eq^{n}.

$$[\mathrm{Mo}'_{\mathrm{Mo}}] \rightarrow [La_{\mathrm{Sr}}^{\bullet}] + 2[\mathrm{V}_{\mathrm{o}}^{\bullet\bullet}] \quad (5.8)$$

The donor doping of La^{3+} substituting for Sr^{2+} can be charge balanced by the decrease of oxygen vacancy concentration and/or the increase of electronic charge $\mathrm{Mo}'_{\mathrm{Mo}}$concentration. The increase in electronic conductivity is attributed to increase of electronic charge $\mathrm{Mo}'_{\mathrm{Mo}}$concentration which can be confirmed by eq^{n}. (5.8). This result provides good agreement with low value of activation energy (~0.29 eV) in reducing atmosphere.

5.2.2 Conclusion

The electrical and structural behaviour La^{3+} substituted double perovskite system, $Sr_{2-x}La_xNiMoO_{6-\delta}$ (x = 0.02, 0.04, 0.06, 0.08, and 0.10), synthesized by citrate-nitrate auto-combustion route were studied. The Rietveld analysis of the X-ray data confirmed phase formation with a minor impurity phase of $SrMoO_4$. The impurity phase plays an important role to control the lattice parameters. The microstructural analysis of the SEM investigation confirmed the fine grains having sizes in the micrometer range. The electrical properties showed that the doping affects the conduction behaviour. The conductivity was found to show initial increasing trend up to x=0.04 thereafter, a decreasing trend for the higher dopant compositions was observed. The compositions with x=0.04 showed higher conductivity due to maximum reduction of Mo^{6+} in Mo^{5+}. Also, it is predicted that the low lattice strain in this composition may cause lower charge polarization leading to high conductivity. The detailed study of XPS data of the compositions also confirmed the reduction of Mo^{6+} in Mo^{5+}. The decreasing trend of the conductivity for the compositions with x > 0.04 was found due to formation of associate pairs, which leads to decrease in effective number of charge carriers contributing to the conduction process. The thermal analysis by DSC/TG of the samples also supports the reduction process in system. SLNM04 shows a conductivity value of 0.1 Scm^{-1} at 600 °C in H_2 atmosphere, which is quite high and may be suitable for anode application in SOFC.

5.3 Section-II: Structural and the Electrical properties Rare Earth (Ce^{3+}) Doped Sr_2NiMoO_6 as Anode System

The abbreviations for the system $Sr_{2-x}Ce_xNiMoO_6$ with x = 0.01, 0.02, 0.03, 0.04 and 0.05 are SCNM01, SCNM02, SCNM03, SCNM04, and SCNM05, respectively. Compositions, $Sr_{2-x}Ce_xNiMoO_{6-\delta}$ with $0.01 \leq x \leq 0.05$ were prepared via earlier mentioned citrate nitrate auto-combustion synthesis route (as elaborated in section 2.3.2.2, (c) of chapter 2). All prepared samples were characterized by XRD, DSC/TG, SEM, XPS and electrochemical impedance technique.

5.3.1 Results and Discussion

5.3.1.1 XRD Study

The phase and crystal structure of the system $Sr_{2-x}Ce_xNiMoO_{6-\delta}$ were determined by powder X-ray diffraction technique at room temperature. Figures 5.13(a)-(e) show the X-ray diffraction patterns of the system $Sr_{2-x}Ce_xNiMoO_{6-\delta}$ with $0.01 \leq x \leq 0.05$. The XRD peak profiles of the prepared samples reveal crystalline nature of the material. The observed peaks of major phase could be pointed out on the basis of double perovskite tetragonal phase $Sr_{2-x}CexNiMoO_{6-\delta}$ with space group *I4/m* using JCPDS card no.15-0601. A few traces of impurities were investigated in the X-ray diffraction pattern of the system $Sr_{2-x}Ce_xNiMoO_{6-\delta}$. The impurity phases were identified as tetragonal $SrMoO_4$ phase (s. g. *I41/a*) using JCPDS card no. 85-0586 and cubic CeO_2 phase (s. g. *Fm*3*m*) using JCPDS card no. 04-0835. Only impurity phase $SrMoO_4$ was detected in the sample with x=0.01 while in the samples x = 0.02, 0.03, 0.04 and 0.05 both phases ($SrMoO_4$ and CeO_2) were observed. The impurity phases $SrMoO_4$ is common in this system and has already been reported in literature [Kumar et al. (2015)].These are indicated with asterisk symbols in Fig.5.13. The average crystallite size for all powder samples was determined from the high intense Bragg's peak corresponding to (200) reflection using Scherrer's formula

$$D = 0.9\lambda/\beta_c \, Cos\theta \qquad (5.9)$$

where λ is the wavelength of X-ray, β_c is corrected full width at half maxima of the diffraction peak and θ is Bragg's diffraction angle. The average crystallite size for all compositions is given in Table5.4. The Rietveld refinement of XRD data for all SCNM-x samples is also shown in Fig.5.13 (a)-(e).

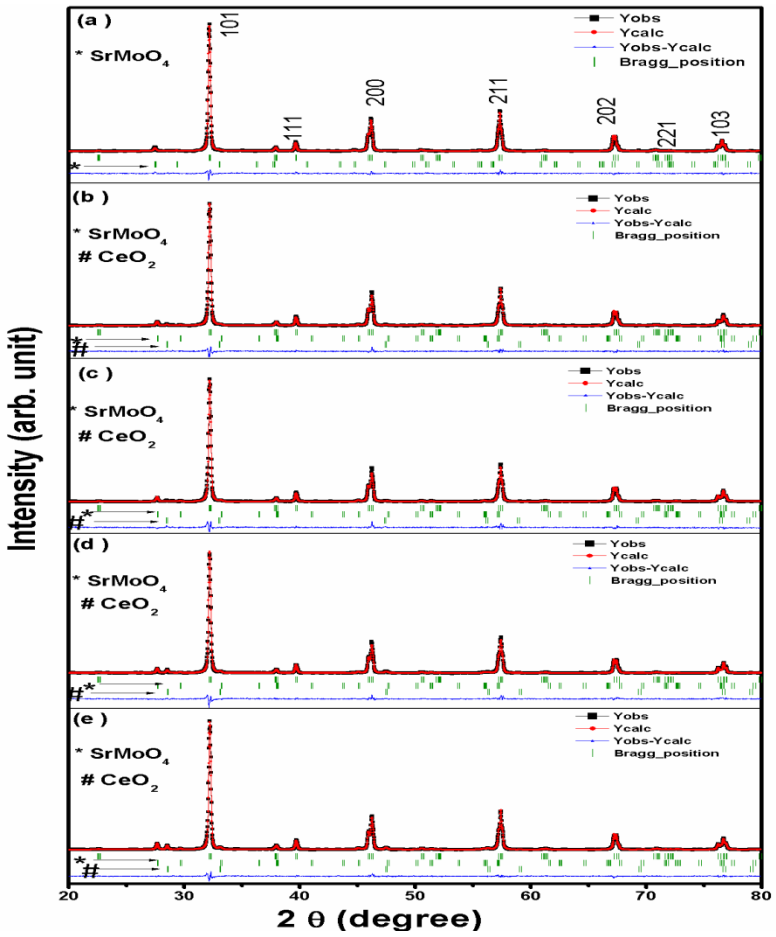

Fig.5.13: *Rietveld refinement of X-ray diffraction pattern of samples* ***(a)*** *SCNM01,* ***(b)*** *SCNM02,* ***(c)*** *SCNM03,* ***(d)*** *SCNM04 and* ***(e)*** *SCNM05. Here Yobs, Ycal, and Yobs-Ycal represent the experimental data, calculated data, and the difference of experimental and calculated data, respectively.*

The refinement was carried out applying *FullProf* software and the refined parameters of the system are mentioned in Table5.4. In the refinement process, the peak profiles were modelled with pseudo-Voigt function along with the six coefficient polynomial background. χ^2 was taken as numerical criterion for the quality of the fit between experimental and calculated diffraction patterns. The refined lattice parameter and χ^2 value of the system are given in Table 5.4. This table shows that the cell parameters for all the samples are almost constant except the sample SCNM01 for which it is maximum. A slight change in lattice parameter is due to smaller ionic radius of Ce^{3+} (1.02 Å) as compared to Sr^{2+} (1.18 Å) [Shannon et al. (1976)]. Parameters of the investigated system are mentioned in Table5.4. In the refinement process, the peak profiles were modelled with pseudo-Voigt function along with the six coefficient polynomial background. χ^2 was taken as numerical criterion for the quality of the

fit between experimental and calculated diffraction patterns. The refined lattice parameter and χ^2 value of the system are given in Table5.4. This table shows that the cell parameters for all the samples are almost constant except the sample SCNM01 for which it is maximum. A slight change in lattice parameter is due to smaller ionic radius of Ce^{3+} (1.02 Å) as compared to Sr^{2+} (1.18 Å) [Shannon et al. (1976)]. This observed change in volume fraction will be discussed in explaining the conductivity behavior in the forthcoming section.

Table.5.4: *Variation in lattice parameters of SCNM-x (x = 0.01, 0.02, 0.03, 0.04 and 0.05) system.*

Samples	Lattice Parameters			Crystallite Size (nm)	χ^2	% of volume fraction of $SrMoO_4$	% of volume fraction of CeO_2
	a (Å)	b = c (Å)	Cell Volume $(Å)^3$				
SCNM01	5.55669	7.89812	243.869	73.52	4.64	2.74	0.00
SCNM02	5.54978	7.89498	243.166	73.29	5.42	2.00	0.56
SCNM03	5.5503	7.8963	243.251	71.02	7.97	2.96	0.86
SCNM04	5.54903	7.89498	243.100	71.98	5.38	3.37	1.51
SCNM05	5.5493	7.8950	243.128	65.81	3.79	3.81	1.79

5.3.1.2 TG/DSC Analysis

The TG/DSC measurements were carried out between room temperature and 1000 ºC under N_2 atmosphere. Figure 5.14 shows the typical TG/DSC curves of the sample SCNM01. During heating two steps of weight loss at 500 °C and 800 °C were observed. The first weight loss at 500 °C may be attributed to loss of oxygen and the second weight loss at around 800 °C may be accounted for the formation of more oxygen vacancies under the reduction of Mo^{6+} in to Mo^{5+} [Huang et al. (2009)].

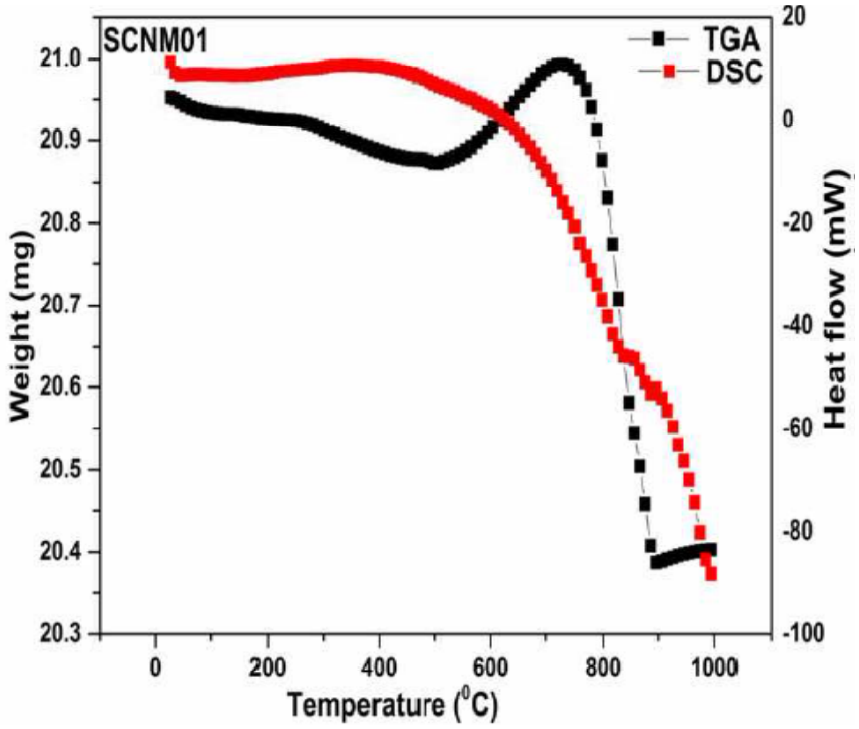

Fig.5.14: *TGA/DSC curve for SCNM01 in N_2 atmosphere.*

5.3.1.3 SEM Study

Scanning electron micrographs were employed to evaluate the surface morphologies of the samples. Figure 5.15(a)–(e) show SEM images of conducting samples sintered at 1300 °C. The SEM images of the compositions show the formation of slightly porous materials with fine grains. The average grain size of the samples SCNM01, SCNM02, SCNM04, and SCNM05 was found approximately ~5.2 µm, ~2.8 µm, ~3 µm, ~3.1 µm and ~3.2 µm, respectively. This trend of average grain size can be correlated with the presence of impure phase in the samples. From the Table.5.5, it can be seen that sample SCNM01 has only impure phase $SrMoO_4$ and hence, it has bigger average grain size. Whereas other samples have impure phases $SrMoO_4$ and CeO_2 and have smaller average grain size in comparison to SCNM01. Also the samples SCNM02, SCNM03, SCNM04 and SCNM05 have shown gradual increase in average grain size. In this regard, phase $SrMoO_4$ plays an important role to increase the average grain size, but phase CeO_2 play inverse role. The combined effect of these two phases result the trend of the observed variation of average grain size with composition.

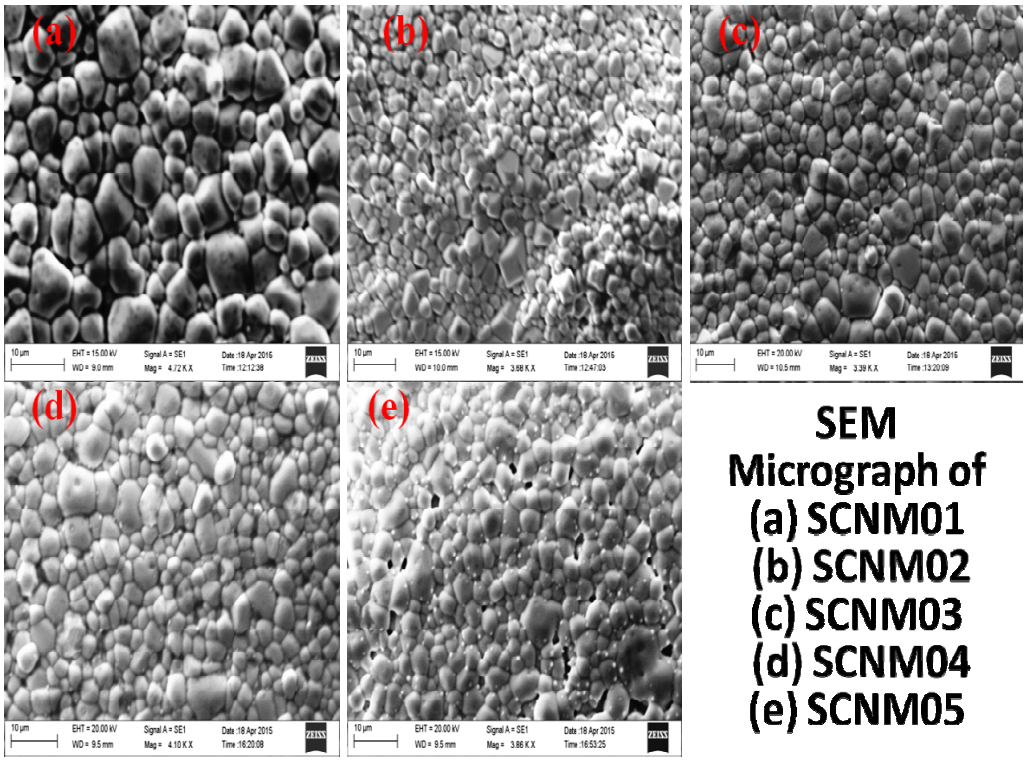

Fig.5.15: *Field emission scanning electron micrograph of chemically etched samples* ***(a)*** *SCNM01,* ***(b)*** *SCNM02,* ***(c)*** *SCNM03,* ***(d)*** *SCNM04 and* ***(e)*** *SCNM05.*

5.3.1.4 XPS Study

The XPS analysis has been done to distinguish the type of charge carriers present in a particular composition of the system SCNM-x. The XPS spectrum images corresponding to Mo and O of SCNM-x samples are schematically shown in Fig.5.16 (a)-(b). The XPS data has been calibrated with respect to standard C 1s peak appeared at 284.6 eV. Figure 5.16(a)-(b) give a picture of the complex Lorentzian peak fitting of elevated peaks. Figure 5.16 (a) clearly depicts that Mo-3d spectra are splitting into two asymmetrical peaks for all the compositions. The binding energies of ions for SCNM-x samples for corresponding states Mo (3d), and O (1s) are mentioned in Table 5.5.These detected asymmetrical peaks of Mo (3d) could be fitted into two pairs that are allocated to $3d_{5/2}$ and $3d_{3/2}$ levels corresponding to Mo^{6+} and Mo^{5+} states, respectively [Xie et al. (2014)]. The XPS analysis reveals that the ratio of Mo^{5+}/Mo^{6+} is at variance with Ce^{3+} substitution on Sr^{2+} site that was determined by the ratio of the integrated area of the peaks corresponding to both states. The peak profiles explaining the each peak for all the samples are given briefly in Table5.5. The composition SCNM01 has the lowest value of ratio of $Mo^{5+/}Mo^{6+}$ among of all prepared samples. Figure 5.5 (b) shows the peaks of O-1s

core level spectra, these spectra are represent the broader and asymmetrical nature for all the samples.

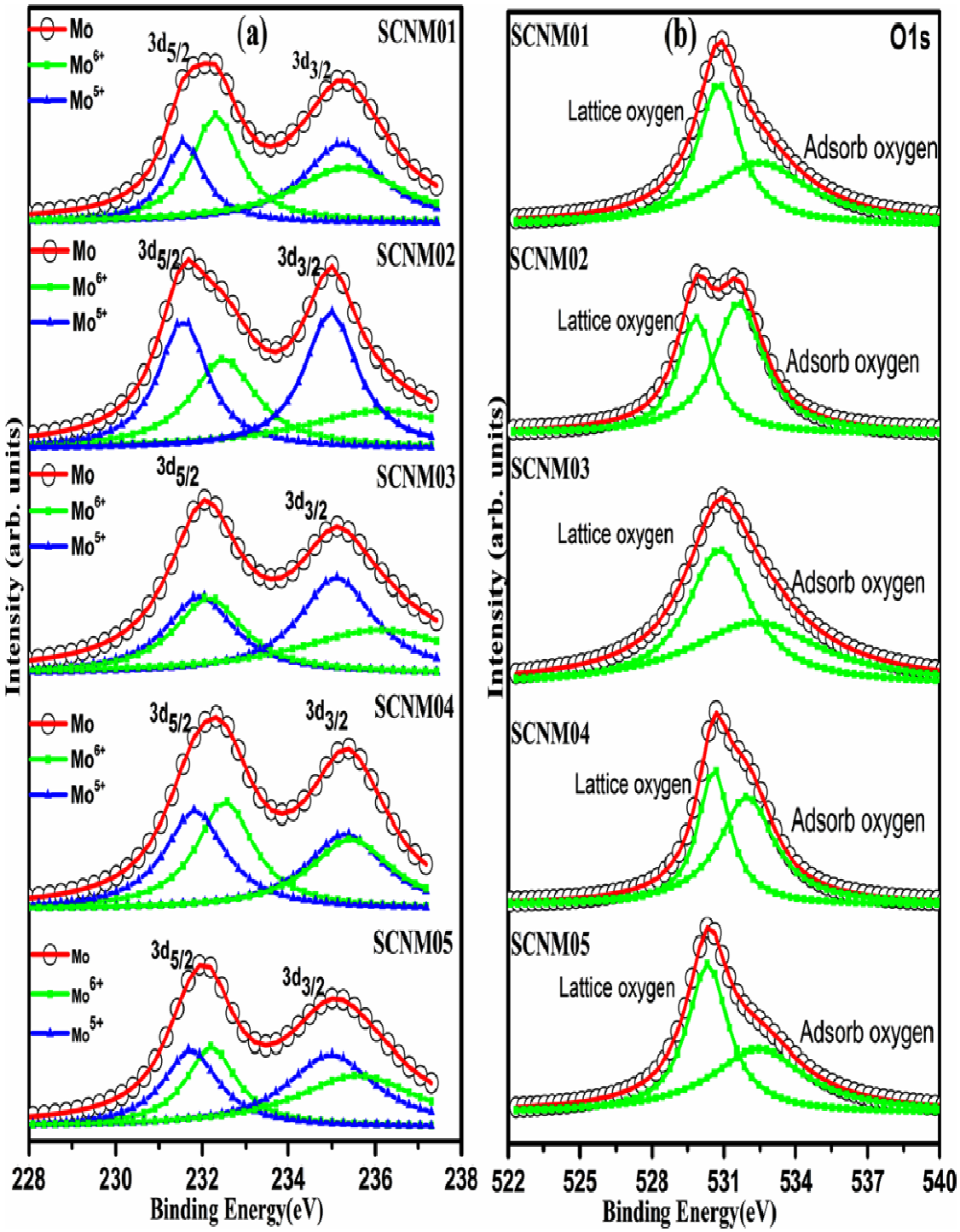

Fig.5.16: *XPS spectra for compositions SCNM01, SCNM02, SCNM03, SCNM04 and SCNM05:* ***(a)*** *Mo-3d and* ***(b)*** *O-1s.*

Table5.5. *The XPS fitting results of Mo-3d spectra and percentage of adsorbed oxygen of the system SCNM-x ($0.01 \leq x \leq 0.05$).*

Compositions	Parameters	Mo^{6+}		Mo^{5+}		Mo^{5+}/Mo^{6+}	Adsorbed oxygen %
		$3d_{5/2}$	$3d_{3/2}$	$3d_{5/2}$	$3d_{3/2}$		
SCNM01	Binding Energy(eV)	232.29	235.38	231.50	235.25	0.82	49.10
	Area	2544.06	2967.95	1562.17	2963.83		
SCNM02	Binding Energy(eV)	232.47	235.78	231.57	235.02	1.10	54.60
	Area	1842.65	1920.74	1943.32	2230.05		
SCNM03	Binding Energy(eV)	232.13	235.88	231.86	235.12	0.99	50.58
	Area	2135.97	2900.07	2138.30	2868.42		
SCNM04	Binding Energy(eV)	232.60	235.42	231.84	235.44	0.98	58.18
	Area	5480.67	5251.26	5251.26	5122.57		
SCNM05	Binding Energy(eV)	232.23	235.48	231.70	235.05	1.15	47.40
	Area	1831.19	2296.56	1533.14	3219.11		

These peaks are fitted corresponding to two kinds of oxygen varieties, Viz, lattice oxygen and adsorbed oxygen. The adsorbed oxygen percentages are also given in Table5.5. This result depicts that on Ce^{3+} substitution the percentage of adsorbed oxygen increases for compositions SCNM02 and SCNM04, on further Ce^{3+} substitution, the adsorbed oxygen percentage decreases for SCNM03 and SCNM05. The reduction of Mo^{6+} is arrtibuted to oxygen vacancy which was determined by the ratio of the integrated area of the peaks corresponding to appropriate states. The Ce^{3+} substitution on Sr^{2+} site releases the charge carrier concentration [$Mo^{5+}_{Mo^{6+}}{}'$] which plays a key role in conduction mechanism.

5.3.1.5 Electrical conductivity

The electrical conductivity of the all prepared samples was studied applying complex-plane plot of impedance spectra. The resistance of charge transfer is calculated by depressed

semicircular arc under entire frequency range (high to low) of the complex-plane plot of impedance spectra [Agarwal et al. (1992) and Veal et al. (2015)]. The electrochemical impedance plots consist of one or more depressed semicircles. These depressed semicircles represent the contribution of grain, grain-boundary and electrode polarization [Hodge et al. (1976)]. As a representative, the impedance spectra for the composition SCNM01 is shown in Fig 5.17 (a)–(d) at a few temperatures in the entire measured frequency range.

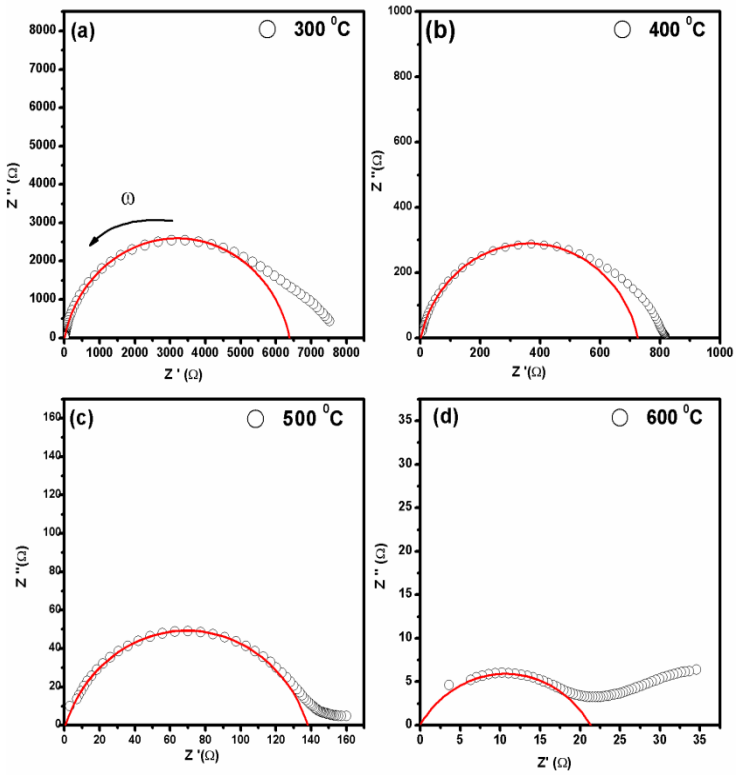

Fig.5.17 *The complex plane Impedance plots for the sample SCNM01 at* ***(a)*** *300 °C,* ***(b)*** *400 °C,* ***(c)*** *500 °C, and* ***(d)*** *600 °C.*

This figure illustrates the fitted data applying nonlinear least squares fitting to the Nyquist plot of real impedance (Z′) vs. imaginary impedance (Z″). From the above figure, it can be seen that only one depressed semicircular arc is observed with a tail. The value of capacitance C for the above observed depressed semicircular arc was calculated using the relation $2\pi RC = 1$, which holds good at the peak point of the depressed semicircular arc where R, C and ω are the resistance, capacitance and angular frequency, respectively. The value of capacitance C was found to be of order of nano farad. This value of capacitance indicates the contribution from the grain boundary. As a representative, the corresponding modulus spectra for the

impedance spectra the composition SCNM01 is shown in Fig5.18 at the temperatures where the impedance spectra are given.

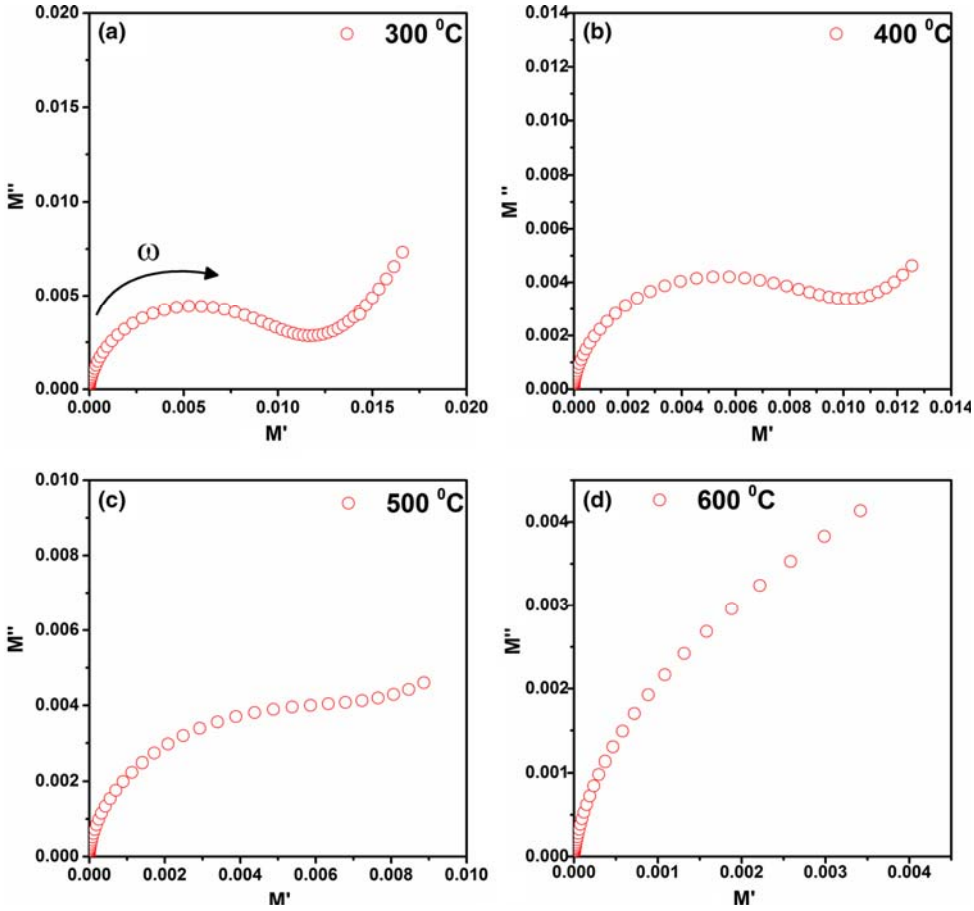

Fig.5.18 *Complex-plane modulus plots for the sample SCNM01 at* ***(a)*** *300 °C,* ***(b)*** *400 °C,* ***(c)*** *500 °C and* ***(d)*** *600 °C.*

From the above figure it can be seen that only one depressed semicircular arc is observed with a tail. The value of capacitance for this depressed semicircular arc was also calculated in the same manner as described above and found to be of order of pico farad. This value of capacitance indicates the contribution from the grain. The observed both depressed semicircular arc corresponding to impedance spectra and modulus spectra pass through the origin. A minute analysis of both the arc indicates that these two arcs are same and represent the combined contribution of grains and grain-boundaries as the difference in the order of capacitance for both the arcs is reasonable. The reason behind this is that in impedance spectra the more resistive contribution dominates while in modulus spectra less capacitive contribution dominates [Hodge et al. (1976)].

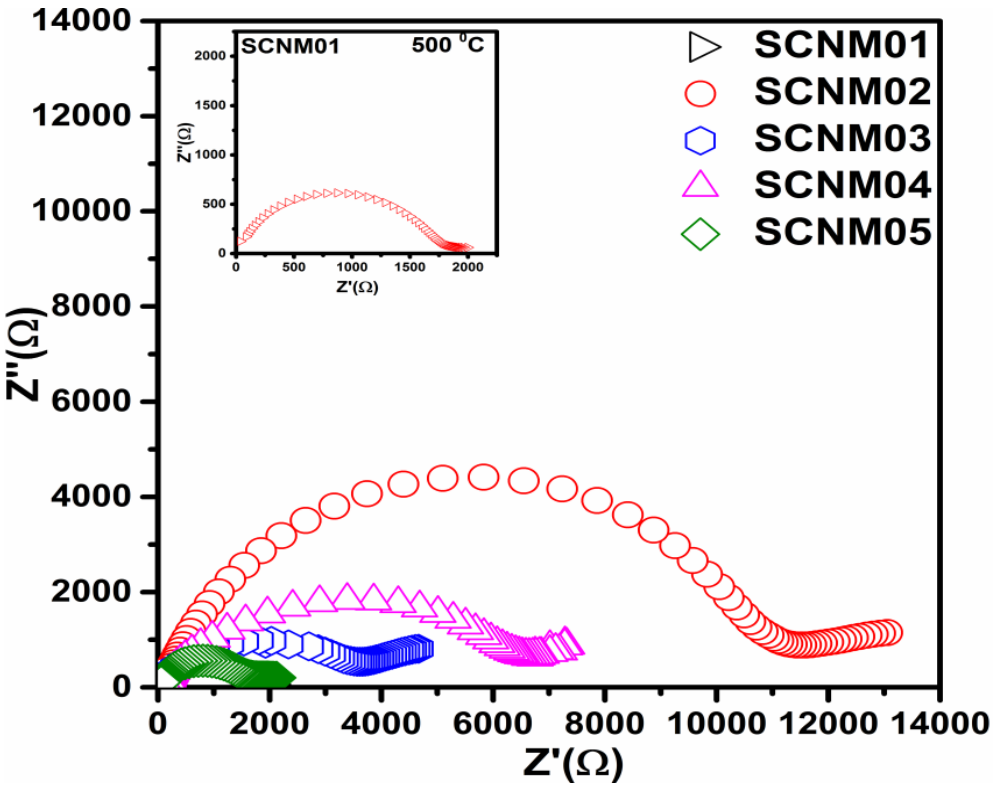

Fig.5.19 *The complex plane Impedance plots for samples compositions SCNM01, SCNM02, SCNM03, SCNM04 and SCNM05 at 500 °C.*

Thus, impedance spectra reflect the capacitance corresponding to grain-boundaries and modulus spectra reflect the capacitance corresponding to grains. The above analysis shows that each depressed semi circular arc in cole-cole plot arises due to combined contributions of grain and grain boundary. Thus the intersection of the semicircular arc on real axis (X-axis) represents the total conductivity of the system at a given temperature.

To observe the effect of doping the on the impedance spectra, the cole-cole plots at 500 °C for all composition are given in Fig.5.19. For clarity, the impedance spectra for the composition SCNM01 is shown in the inset of Fig.5.19. From this figure it can be concluded that the sample SCNM01 has lower impedance than that of the other samples. The value of total resistance, Rt has been obtained by the intercept of the observed depressed semicircular arc with the real axis using the Nyquist plot of real impedance (Z′) vs. imaginary impedance (Z″).The total conductivity of the samples was calculated using equation (5.1). Figure 5.20 shows the plots in $\log\sigma_t T$ and 1000/T for the all samples of system SCNM-x, which represents the Arrhenius behavior. The activation energy was calculated from the slope of the above plot applying the Arrhenius relation (equation 5.2). From this figure, it is clear that the sample

SCNM01 has highest electrical conductivity than the other samples. The calculated value of activation energy E_a for all samples is given in Table.5.6.

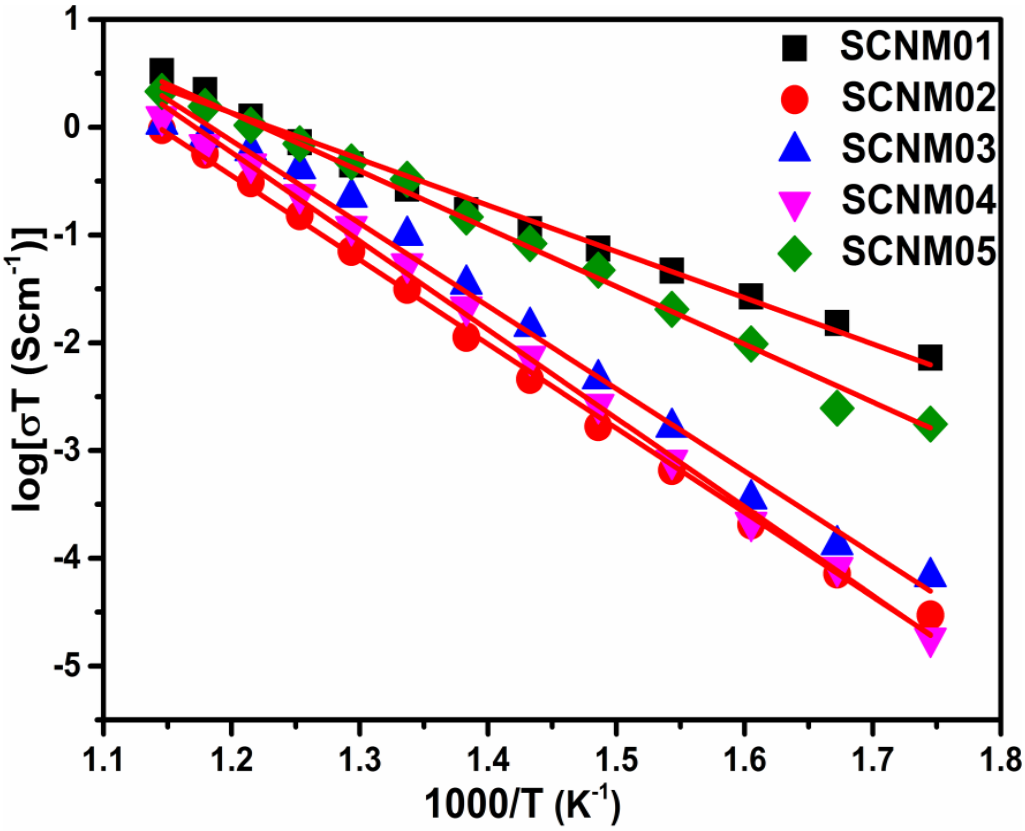

Fig.5.20: *log $\sigma_t T$ vs. 1000/T plots for the system SCNM-x ($0.01 \leq x \leq 0.05$).*

This table also reflects the lowest activation energy for the sample SCNM01. The electrical conductivity in system SCNM-x can be understood using defect chemistry. The doping of Ce^{3+} at Sr^{2+} site in system SCNM-x can be illustrated from following defect equations.

$$Ce_2O_3 \xrightarrow{SrO} 2Ce_{Sr}^{\bullet} + 2e' + O_O^{\times} + \frac{1}{2} O_2 \quad (5.10)$$

$$Mo_{Mo}^{\times} + e' \rightarrow [Mo_{Mo^{6+}}^{5+}{}'] \quad (5.11)$$

Thus the reduction of Mo^{6+} to Mo^{5+} produces electronic charge carriers, resulting in good electronic conduction and lower activation energy. For the samples with x > 0.01 the electrical conductivity is found to be low. This decrease in conductivity may be due to increased impurity phases. But at higher temperature more oxygen vacancy will be created due to loss of oxygen and contributed oxide ion conduction. Huang et al. [2006] and Ullmann et al.[2000] also reported that each oxygen vacancy reduces Mo^{6+} to Mo^{5+} which supports to

increase in the concentration of [$Mo^{5+}_{Mo^{6+}}$′] ions. This would also suppress the reduction of Mo^{6+} to Mo^{5+} and hence production of electronic charge. This would result in lower electronic contribution to the electrical conductivity.

Table 5.6: *Activation energy of SCNM-x (x = 0.01, 0.02, 0.03, 0.04 and 0.05) system.*

Compositions	Temperature Range	E_a(eV) from log(σT) vs. 1000/T plot
SCNM01	300°C - 600 °C	E_a = 0.85
SCNM02	300°C - 600 °C	E_a = 1.6
SCNM03	300°C - 600 °C	E_a = 1.5
SCNM04	300°C - 600 °C	E_a = 1.6
SCNM05	300°C - 600 °C	E_a = 1.1

5.3.1.6 Conductivity measurement of Ce^{3+} doped Sr_2NiMoO_6 in reducing atmosphere

Figure 5.20 discerns that the composition SCNM01 shows the highest conductivity amongst all the prepared samples of cerium doped series in air. Hence it was considered worthwhile to measure the electrical conductivity of SCNM01 in reducing atmosphere. Figure 5.21 demonstrates the plot of resistance as function of temperature for Sm^{3+} doped Sr_2NiMoO_6 (SSNM05) system in reduced H_2 atmosphere, which was measured in temperature range of 100-600 ^{0}C during the cooling cycle. This figure clearly shows that resistance value decreases with increasing of temperature and get low value above 500 °C. The electrical conductivity of samples measured in air as well as reducing atmosphere in the temperature range of 300-600 °C is shown in Fig5.22. The highest electrical conductivity is obtained 0.23 Scm^{-1} at 600 °C, which is 98.6 % higher than that of in air. The influence of reducing temperature on the electrical conductivity of sample SCNM01 is shown in Fig.5.22**.** The electrical conductivity of SCNM01 increases significantly with increasing reducing temperature as compared to that in air. The activation energy (E_a) of SCNM01 sample for electron transportation is extracted from Arrhenius plots and found to be 0.82 eV and 0.21eV in air and H_2, respectively. It can be seen that the value of E_a in reducing atmosphere is considerably smaller than that of its value in air. Vasala et al. (2011) reported that $SrMoO_4$ phase was found in Sr_2MgMoO_6 during the

synthesis process but in reducing condition $SrMoO_4$ is reduced to $SrMoO_3$ which play key role to enhance the electrical conductivity and hence lowering the activation energy.

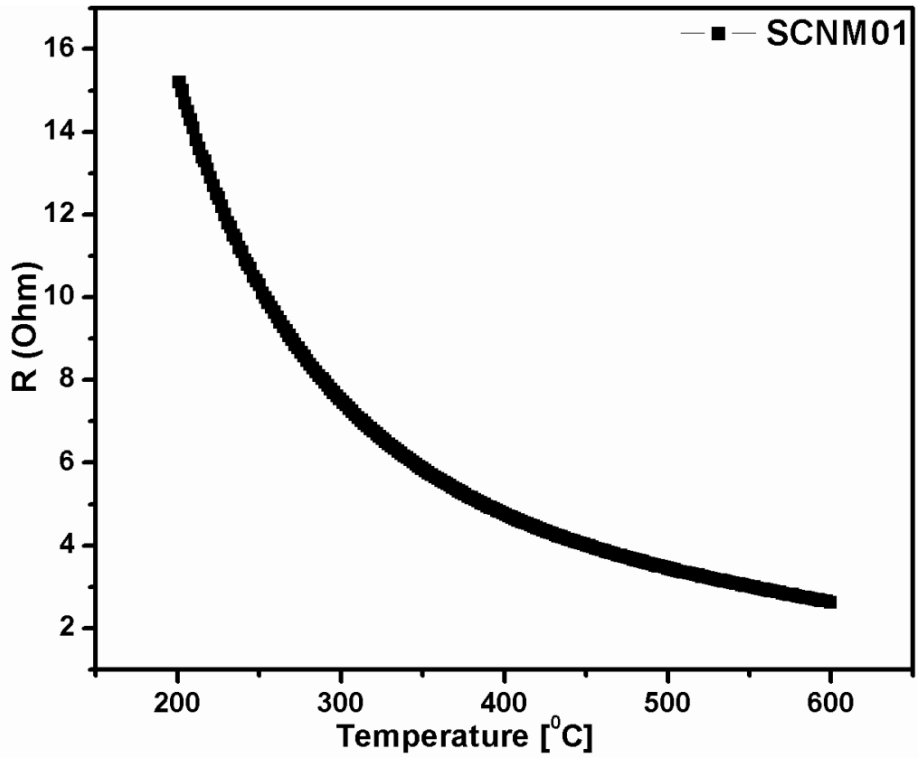

Fig.5.21. *The plots of Resistances (R) vs. Temperature for the $Sr_{1.99}Ce_{0.01}NiMoO_{6-\delta}$ (SCNM01) sample in H_2 atmosphere.*

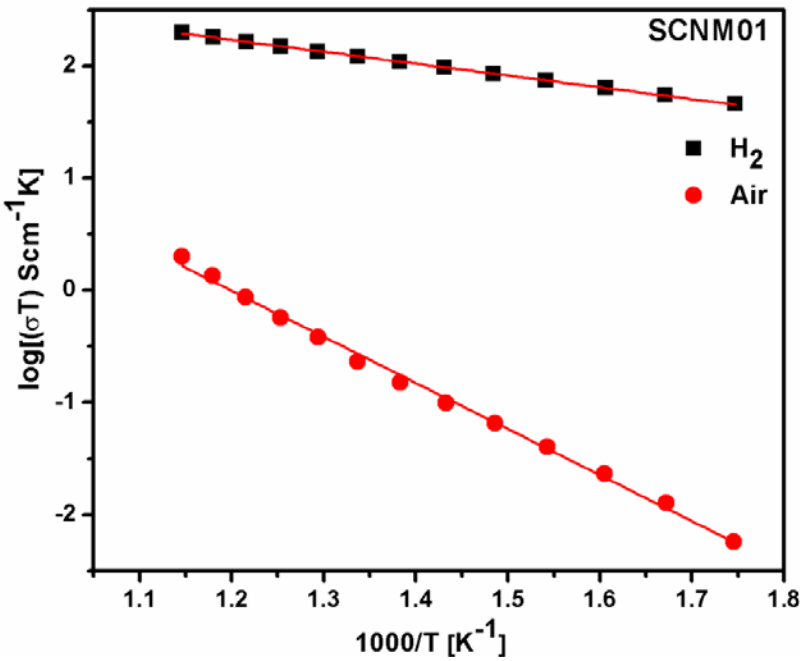

Fig.5.22. *Arrhenius plots of conductivity for the SCNM01 sample in H_2 and air atmosphere.*

Rare earth (Ce^{3+}) substitution on Sr^{2+} site in Sr_2NiMoO_6 system represents the increase in electrical conductivity in reducing atmosphere (H_2) which can be studied from following defect Eqs.

$$\left.\begin{array}{l} Ce_2O_3 \xrightarrow{SrO} 2Ce_{Sr}^{\bullet} + 2e' + 2O_O^{\times} + \frac{1}{2}O_2 \uparrow \\ Mo_{Mo}^{\times} + e' \rightarrow Mo_{Mo}' \end{array}\right\} \quad (5.12)$$

where presence of defects in investigated system with donor substitution reveals that the lattice oxygen may be lost under reducing enviournment (H_2) and generate the oxygen vacancies and also the reduction of Mo^{6+} in to Mo^{5+}. This can be explained by following eq^{n}.

$$2Mo_{Mo}^{\times} + O_O^{\times} \rightarrow 2Mo_{Mo}' + V_o^{\bullet\bullet} + \frac{1}{2}O_2(g) \uparrow \quad (5.13)$$

where electronic charge Mo_{Mo}' is resulted by Mo^{5+} substitution on Mo^{6+} site. The charge neutrality is assigned from following eq^{n}.

$$[Mo_{Mo}'] \rightarrow [Ce_{Sr}^{\bullet}] + 2[V_o^{\bullet\bullet}] \quad (5.14)$$

The rare earth, Ce^{3+} substituting for Sr^{2+} can be charge balanced by the decrease of oxygen vacancy concentration and/or the increase of electronic charge Mo_{Mo}'concentration. Eq^{n}. (5.14) indicates the result of decrease of ionic conductivity and enhancement of electronic conductivity.

5.3.2 Conclusions

Double perovskite system $Sr_{2-x}Ce_xNiMoO_{6-\delta}$ (SCNM) with $0.01 \leq x \leq 0.05$ has been prepared successfully with a few minor phases of $SrMoO_4$ and CeO_2. The thermal study shows the loss of oxygen at higher temperatures. Micro-structural studies revealed that for 1% doping of cerium, the grain has bigger size than that of the other samples but for the composition having 2 mole % cerium, grain size decreases and again increases for higher percentage of doping. The XPS study of all compositions predicted the reduction of Mo^{6+} in to Mo^{5+}. The doping of cerium increases the electrical conductivity of the studied system due to the production of electronic charge carriers. It seems that the doping of cerium greater than 1 mole % increases the impurity phase, which results the decrease in electrical conductivity. The sample SCNM01 has highest conductivity with lowest activation energy of 0.85 eV and 0.21eV in air and H_2, respectively. SCNM01 gets better performance of electronic conductivity due to low activation in H_2. It may act as potential anode candidate for SOFC.

5.4 Section-III: Structural and the electrical properties of rare earth (Sm^{3+}) doped Sr_2NiMoO_6 as anode system

The abbreviations for the system $Sr_{2-x}Sm_xNiMoO_6$ with x = 0.01, 0.02, 0.03, 0.04 and 0.05 are SSNM01, SSNM02, SSNM03, SSNM04 and SSNM05, respectively. Series of $Sr_{2-x}SmxNiMoO_{6-\delta}$ system with $0.01 \leq x \leq 0.05$ was prepared via similar route, citrate nitrate auto-combustion synthesis route which was used in chapter-II. These prepared samples were also characterized by XRD, DSC/TG, SEM, XPS and electrochemical impedance technique.

5.4.1 Result and Discussions

5.4.1.1 XRD Analysis

The phase confirmation and crystal structure of the system $Sr_{2-x}Sm_xNiMoO_{6-\delta}$ were determined employing powder X-ray diffraction technique at room temperature. Figure 5.23 (a)-(e) represent the X-ray diffraction patterns of the system $Sr_{2-x}SmxNiMoO_{6-\delta}$ with compositions $0.01 \leq x \leq 0.05$. The observed peaks of major phase could be observed on the basis of double perovskite tetragonal phase $Sr_{2-x}Sm_xNiMoO_{6-\delta}$ with space group *I4/m* using JCPDS card no. 15-0601. Impurities phase is investigated for few compositions in SSNM-x system were identified as tetragonal $SrMoO_4$ phase (s. g. *I41/a*) using JCPDS card no. 85-0586. Based on previous literature survey the presence of impurity phase $SrMoO_4$ is common in this system [Filonova et al. (2014)]. In present investigated system $SrMoO_4$ is observed for compositions SSNM01, SSNM04 and SSNM05 remaining compositions SSNM02 and SSNM03 confirm the single phase formation. The Rietveld refinement of XRD data for all SSNM-x samples is also shown in Fig.5.23 (a)-(e). Lattice parameters determined by XRD patterns using Rietveld refinement is shown in Table.5.7. It can be observed that lattice parameters decreases upto SSNM04, and afterward slightly decrease for composition. This impurity phase is also detected from Rietveld refinement and indicated with asterisk symbols in Fig.5.23. From Rietveld refinement, the peak profiles were modelled by pseudo-Voigt function by considering the six coefficient polynomial background. The Rwp (weighted-pattern factor) and R values (Rp), and $\chi 2$ values indicate that the refinement results are admissible and consistent with the previous published results. The % of volume fraction of SrMoO4 is observed from Rietveld refinement results for compositions SSNM01, SSNM04 and SSNM05 which is motioned in Table5.7. This indicates that SSNM05 composition get higher value of $SrMoO_4$ phase. The decrease in the lattice parameters may be due to

substitution of lower ionic radii of dopant ions Sm^{3+} (0.69 Å) at the place of the larger ionic radii of host ions Sr^{2+} (1.18 Å) and further increase trend for SSNM05 may be due to combined effect of high impure phase and lower ionic radii of dopant ions [Shannon (1976)].

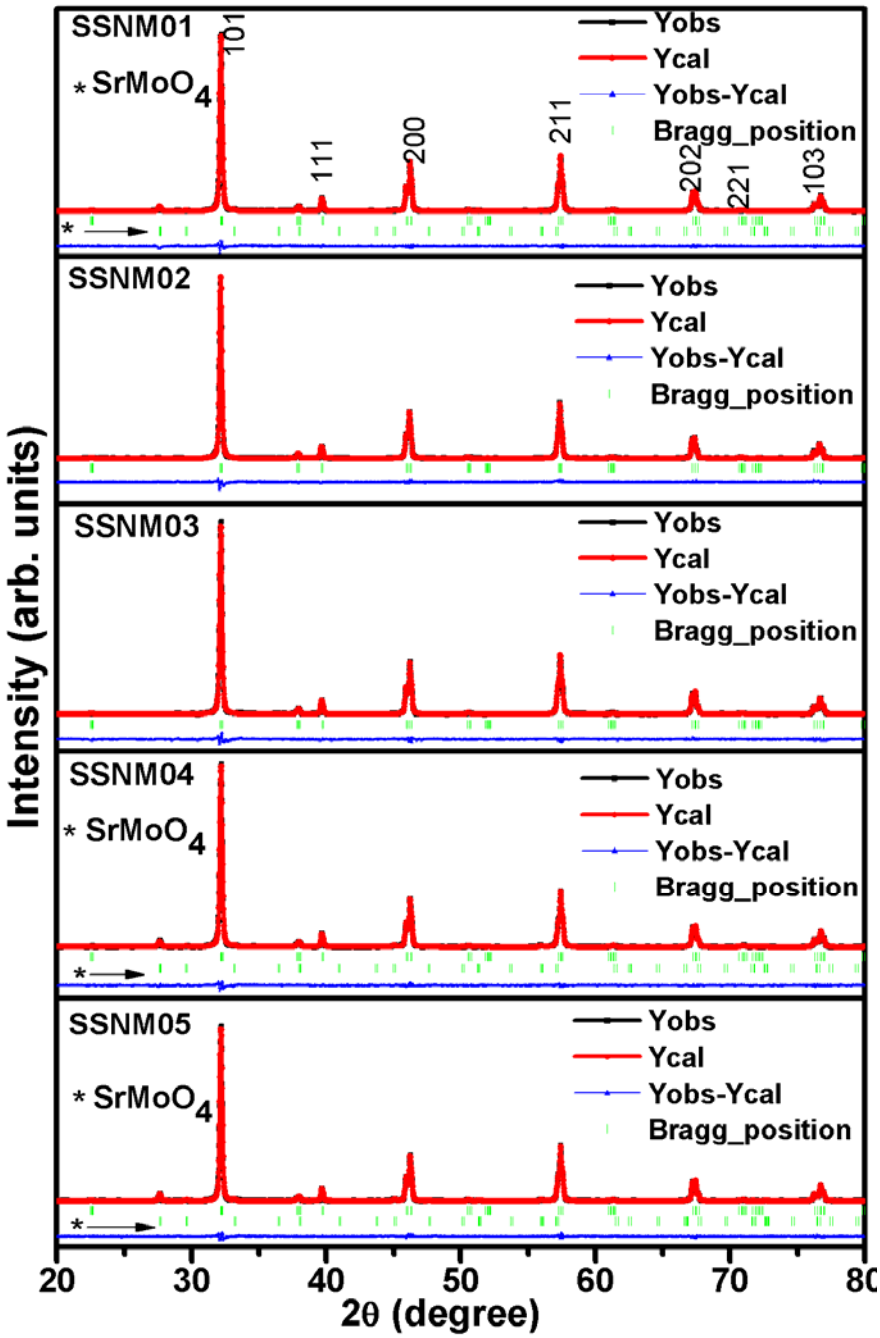

Fig.5.23. *Reitveld refinement of X-ray diffraction pattern of different samples* ***(a)*** *SSNM01,* ***(b)*** *SSNM02,* ***(c)*** *SSNM03,* ***(d)*** *SSNM04 and* ***(e)*** *SSNM05. In this refinement, Yobs, Ycal, and Yobs-Ycal represent the experimental data, calculated data, and the difference of experimental and calculated data, in that order.*

Table.5.7: *Variation in lattice parameters of SSNM-x (x = 0.01, 0.02, 0.03, 0.04 and 0.05) system.*

Samples	Lattice Parameters			R_p	R_{wp}	χ^2	% of volume fraction of $SrMoO_4$
	a (Å)	b = c (Å)	Cell Volume $(Å)^3$				
SSNM01	5.547	7.893	242.91	16.0	13.7	4.92	2.98
SSNM02	5.554	7.894	243.44	16.5	13.0	3.60	0
SSNM03	5.549	7.896	243.16	16.1	12.9	3.73	0
SSNM04	5.547	7.893	242.84	15.4	12.6	3.70	3.43
SSNM05	5.547	7.894	242.91	16	12.8	3.51	4.02

5.4.1.2 TG/DSC Analysis

The TG/DSC analysis was studied from room temperature to 1000 ºC in N_2 atmosphere. Figure 5.24 shows the TG/DSC curves of the sample SSNM01. During heating order two steps of weight loss at 500 ºC and 850 ºC were found.

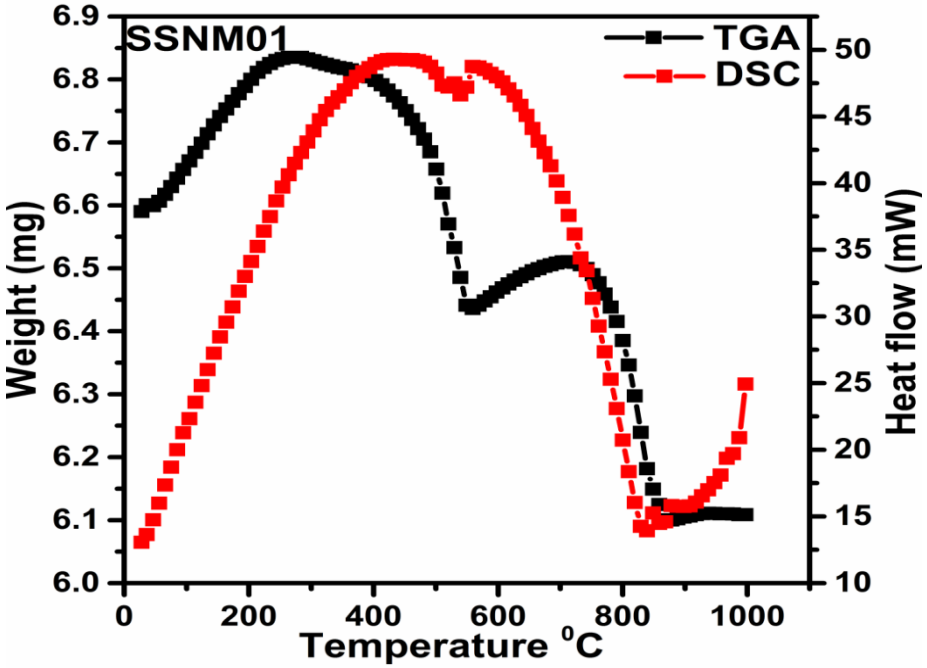

Fig.5.24 *DSC/TG curve for sintered SSNM01 in N_2 atmosphere from RT to 1000 °C.*

The first weight loss at 500 °C may be attributed to loss of oxygen and the second weight loss at around 850 °C may be accounted for the formation of more oxygen vacancies under the reduction of Mo^{6+} in to Mo^{5+} [Huang et al. (2009)].

5.4.1.3 Microstructure Study

The SEM micrograph of all prepared samples has been studied using FESEM after chemically etching. Figure 5.25 (a)–(e) shows SEM images of fractured samples sintered at 1300 °C. The image of SEM reflects that all the samples are compiled with fine grains of irregular shape and size. The average grain size of compositions SSNM01, SSNM02, SSNM03, SSNM04 and SSNM05 calculated by linear intercept method is found to be approximately ~2.36 µm, ~1.59 µm, ~2.89 µm, ~2.38 µm and ~1.49 µm, respectively. At first, grain size decrease for SSNM02 after that increase for SSNM03 and get slight decrease trend downward up to x= 0.05. For higher substitutions i.e x = 0.05, the Sm^{3+} ions segregate at the interface of grain and grain boundaries due to the charge difference and ionic size difference between the Sm^{3+} and Sr^{2+} ions. This segregation further inhibits the grain growth and results a decrease in the grain size [Desu et al.(1990) and Dwivedi et al. (2007)].

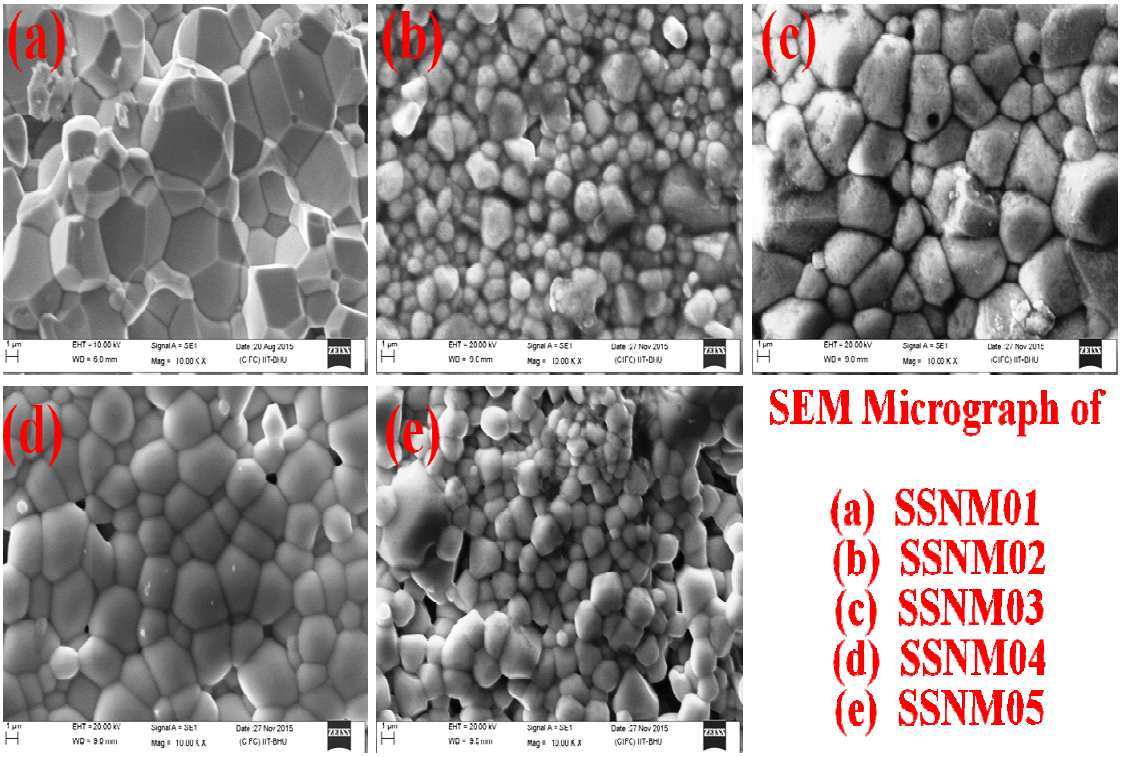

Fig.5.25. *Field emission scanning electron micrograph of fractured compositions (a) SSNM0, (b) SSNM02, (c) SSNM03, (d) SSNM04 and (e) SSNM05.*

5.4.1.4 XPS Analysis

The XPS study has been distinguished the type of charge carriers present in composition of the system SSNM ($0.01 \leq x \leq 0.05$). The XPS spectra corresponding to Mo and O of SSNM-x samples are schematically shown in Fig.5.26 (a)-(b). The XPS data of all compositions has been calibrated with respect to standard C 1s peak appeared at ~284.6 eV. Figures 5.26(a)-(b) show the complex Lorentzian peak fitting of elevated peaks.

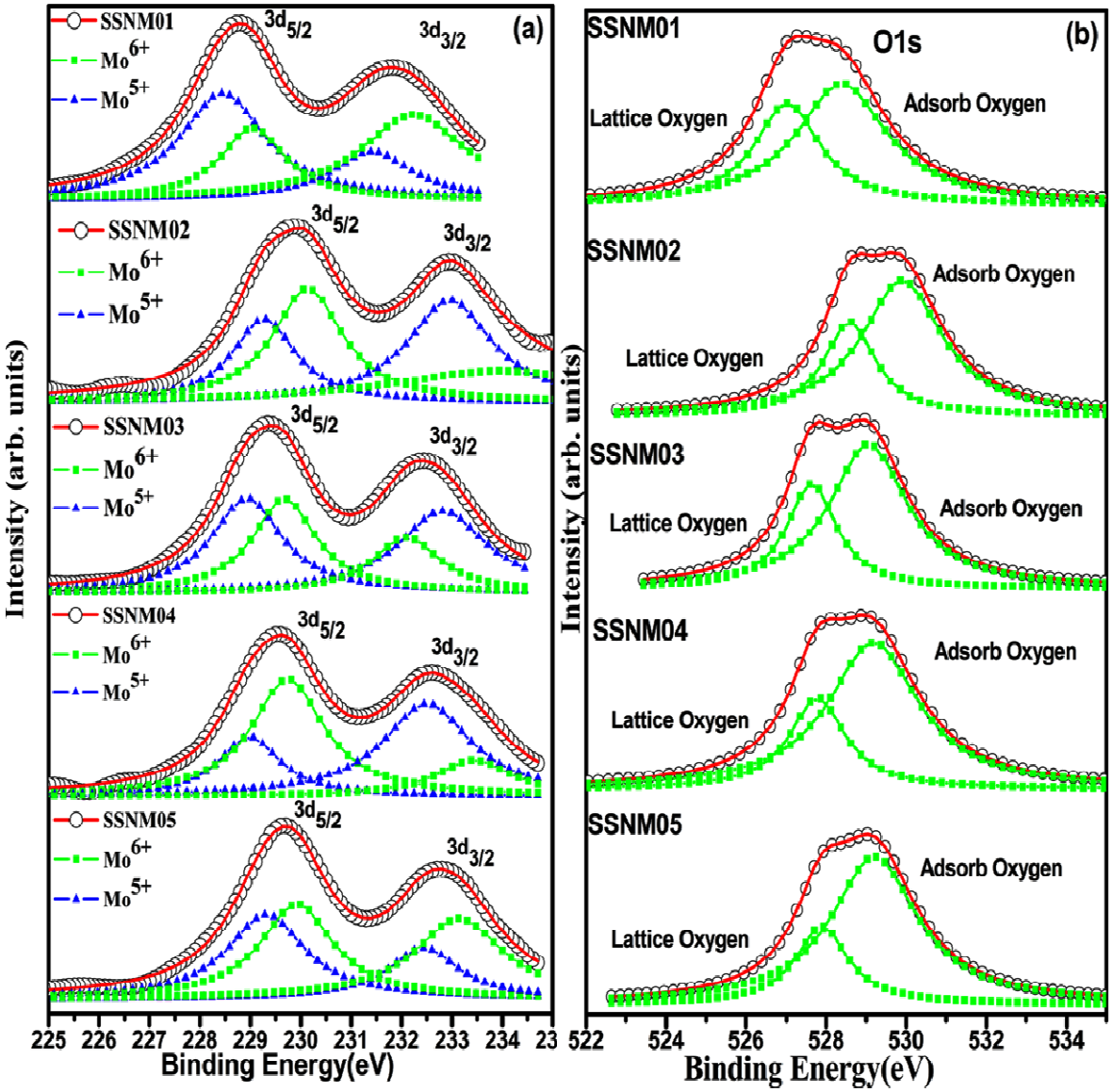

Fig.5.26: *XPS spectra for compositions SSNM01, SSNM02, SSNM03, SSNM04 and SSNM05:* ***(a)*** *Mo-3d and* ***(b)*** *O-1s.*

Figure 5.26 (a) clearly reveals the Mo-3d spectra are splitting into two asymmetrical peaks for all the samples. The XPS result showed that the mixed valence state of Mo^{5+}/Mo^{6+} was found

in each composition. The peak profiles explaining for each sample are given in Table5.8. The composition SSNM05 has the lowest value of ratio of mixed valance $Mo^{5+/}Mo^{6+}$ than all other prepared samples. Figure 5.26 (b) illustrates the peaks of O-1s core level spectra; these spectra are exposed the broader and asymmetrical behaviour in nature for all the compositions. This result finds that with Sm^{3+} substitution the percentage of adsorbed oxygen decreases for all compositions compare to SSNM01 and SSNM05 gets lowest value of adsorbed oxygen percentage. The peaks of oxygen spectra were fitted corresponding to two kinds of oxygen varieties, viz, lattice oxygen and adsorbed oxygen. The calculated adsorbed oxygen percentages are also given in Table5.8. The reduction of Mo^{6+} in to Mo^{5+} is attributed to adsorbed oxygen percentage which was determined by the ratio of the integrated area of the peaks corresponding to appropriate states. To support conduction mechanism, Sm^{3+} substitution on Sr^{2+} site releases the charge carrier concentration [$Mo^{5+}_{Mo^{6+}}{}'$].

Table 5.8. *Fitting results of Mo-3d XPS spectra and percentage of adsorbed oxygen of the system SSNM-x (0.01 ≤ x ≤ 0.05).*

Compositions	Parameters	Mo^{6+}		Mo^{5+}		Mo^{5+}/Mo^{6+}	Adsorbed oxygen %
		$3d_{5/2}$	$3d_{3/2}$	$3d_{5/2}$	$3d_{3/2}$		
SSNM01	Binding Energy(eV)	229.04	232.23	228.45	231.41	0.94	37.71
	Area	3950.35	7572.65	7611.44	3278.46		
SSNM02	Binding Energy(eV)	230.13	5171.29	229.26	232.95	0.93	30.91
	Area	5968.71	5171.29	3930.68	6451.11		
SSNM03	Binding Energy(eV)	229.67	232.09	228.92	232.81	1.42	31.84
	Area	5584.01	3585.02	6206.36	6823.76		
SSNM04	Binding Energy(eV)	229.74	233.43	228.97	232.50	1.05	27.63
	Area	5971.32	1929.81	2539.85	5719.00		
SSNM05	Binding Energy(eV)	229.91	5020.60	229.31	232.44	0.72	24.21
	Area	4850.25	5020.60	4574.56	2522.92		

5.4.1.5 Impedance Analysis

Figure 5.27(a)–(f) shows the impedance spectra for the composition SCNM01 at a few temperatures in the entire measured frequency range. This figure represents the the Nyquist plot of real impedance (Z′) vs. imaginary impedance (Z″) with fitted data applying nonlinear least squares fitting. From figure.5.27 (a)–(f), it can be distinguished that only one depressed semicircular arc is found with a tail.

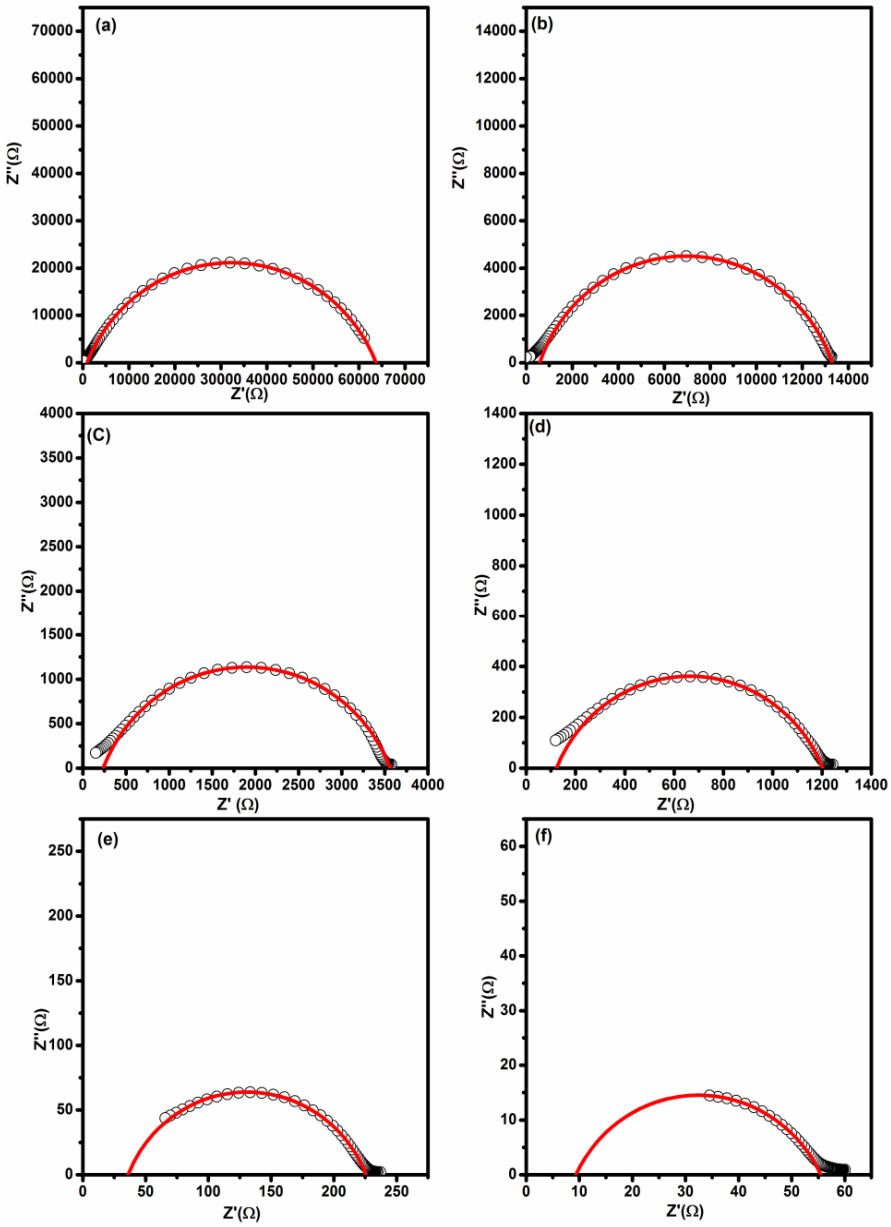

Fig.5.27. *The complex plane Impedance plots for the composition SSNM05:* ***(a)*** *250 °C,* ***(b)*** *300 °C,* ***(c)*** *350 °C,* ***(d)*** *400 °C,* ***(e)*** *500 °C and* ***(f)*** *600 °C.*

The value of capacitance C for the above observed depressed semicircular arc was calculated using the relation $2\pi RC = 1$, which holds good at the peak point of the depressed semicircular arc where R, C and ω are the resistance, capacitance and angular frequency, respectively. The capacitance value observed from depressed semi circle arc was also calculated in the same approach as described above and found to be of order of pico farad. This value of capacitance indicates the combined contribution of grain and grain boundary. To find the effect of doping on the impedance spectra, the cole-cole plots at 450 °C for all composition are given in Fig.5.28. From above figure it can be observed that the sample SSNM05 has lower impedance than that of the other samples. The value of resistance, R has been obtained by the intercept of the observed depressed semicircular arc with the real axis using the Nyquist plot of real impedance (Z′) vs. imaginary impedance (Z″).The total conductivity of the samples was calculated using the equation (5.1).

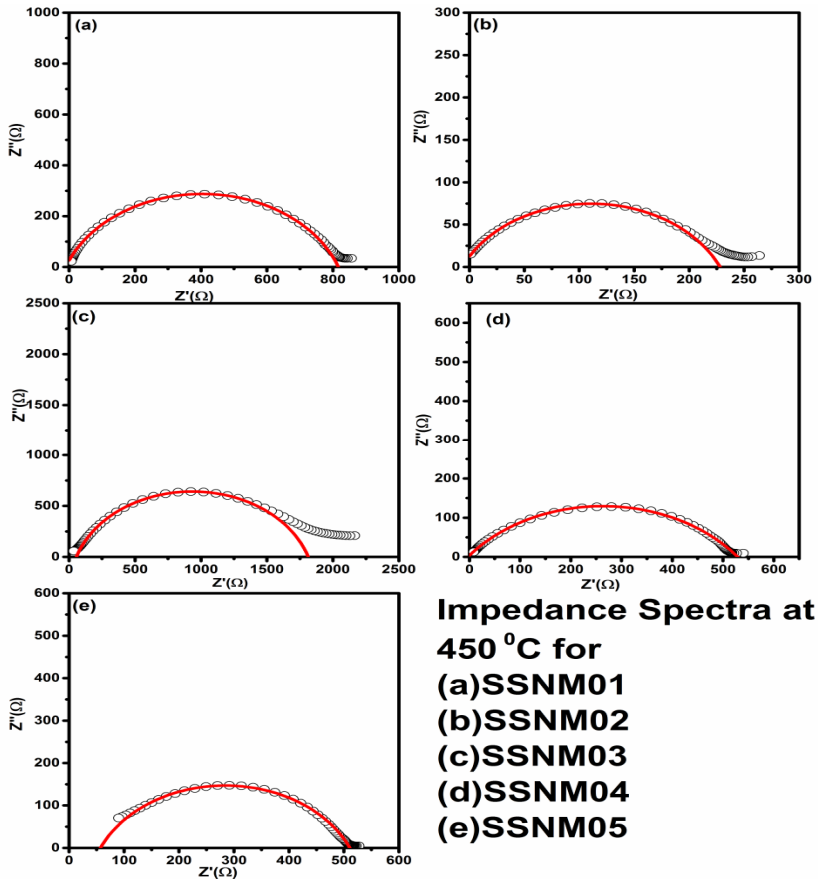

Fig.5.28.*The complex plane Impedance plots for compositions: (a) SSNM01, (b) SSNM02, (c) SSNM03, (d) SSNM04 and (e) SSNM05 (f) combined plot for SSNM-x (0.01≤ x≤0.05): at 450 °C.*

Figure.5.29 shows the plots in logσT and 1000/T for the all samples of system SSNM-x that represents the Arrhenius behavior. The activation energy was calculated from the slope of the above plot applying the Arrhenius relation using equation (5.2).From this figure, it is clear that the sample SSNM05 has highest electrical conductivity than the other compositions. The calculated value of activation energy Ea for all samples is given in Table.9. The result of table also reveals the lowest activation energy for the sample SSNM05. The electrical conductivity of investigated system SSNM-x can be understood using defect chemistry. The doping of Sm^{3+} at Sr^{2+} site in system SSNM-x can be illustrated from following defect equations.

$$\left.\begin{aligned} Sm_2O_3 \xrightarrow{SrO} 2Sm_{Sr}^{\bullet} + 2e' + O_O^{\times} + \frac{1}{2}O_2 \\ Mo_{Mo}^{\times} + e' \rightarrow Mo_{Mo}' \end{aligned}\right\} \qquad (5.15)$$

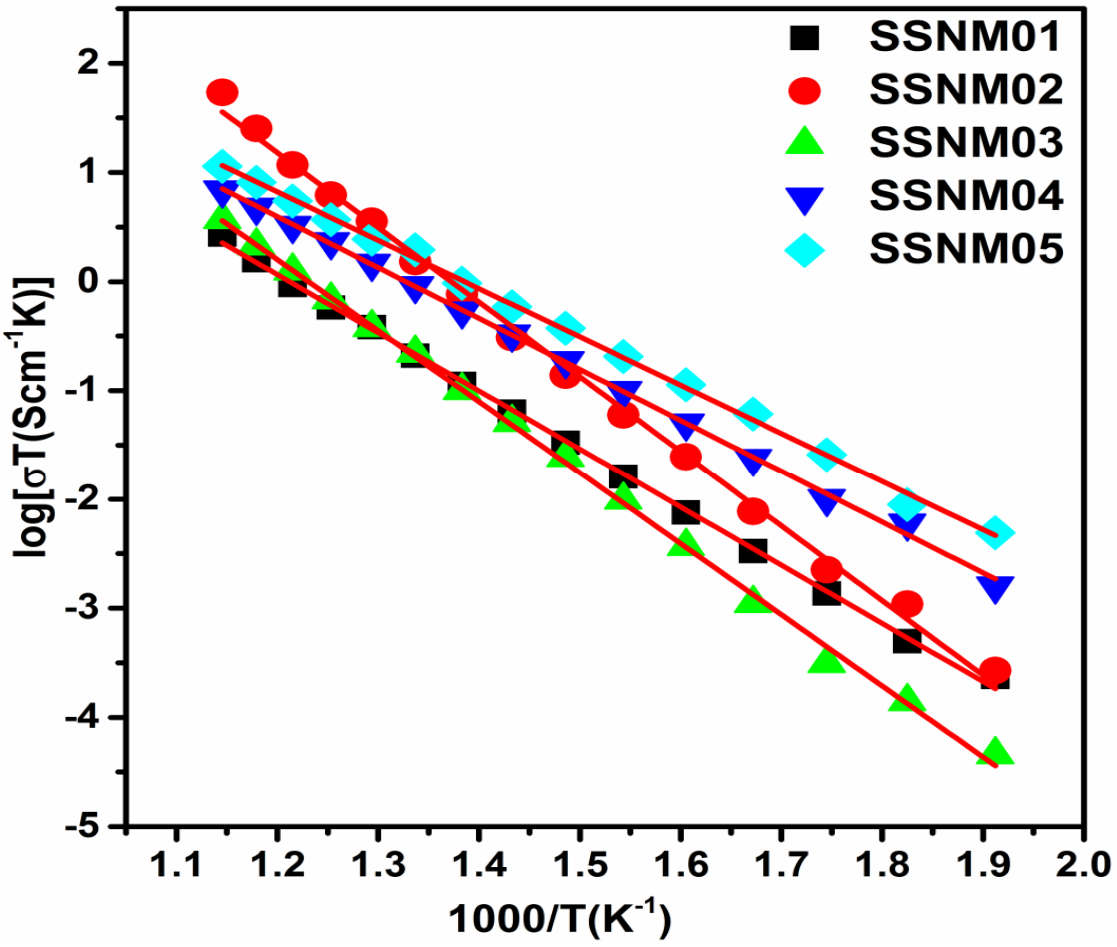

Fig.5.29. *Arrhenius logσT vs. 1000/T plots of various samples of the system SSNM-x ($0.01 \leq x \leq 0.05$).*

Table.5.9. Activation energy of SSNM-x (x = 0.01, 0.02, 0.03, 0.04 and 0.05) system.

Sample	Temperature Range (°C)	Activation Energy E_a from log(σT) vs. 1000/T plot (eV)
SSNM01	200-600	1.06
SSNM02	200-600	1.36
SSNM03	200-600	1.29
SSNM04	200-600	0.92
SSNM05	200-600	0.88

Huang et al. (2009) has been reported that the reduction of Mo^{6+} to Mo^{5+} produces electronic charge carriers, resulting in good electronic conduction and lower activation energy. For the samples with x = 0.05 the electrical conductivity is found to be high. This increase in conductivity may be due to each oxygen vacancy reduces Mo^{6+} to Mo^{5+} which supports to increase in the concentration of [$Mo^{5+}_{Mo^{6+}}{}'$] ions [Huang et al. (2006) and Ullmann et al.(2000)].

5.4.1.6 Conductivity Measurement of Sm^{3+} doped Sr_2NiMoO_6 in reducing atmosphere

Figure 5.29 depicts that the composition SSNM05 shows the highest conductivity amongst all the Sm doped samples. Therefore, it was considered worthwhile to measure the electrical conductivity of this composition in reducing atmosphere. Figure 5.30 shows the plots of resistance as function of temperature for Sm^{3+} doped Sr_2NiMoO_6 (SSNM05) system in reduced H_2 atmosphere that was measured in temperature range of 100-600 °C during the cooling cycle. This figure clearly indicates that resistance value decreases with increasing of temperature and get almost constant above 500 °C. Huang et al. [2009] reported that the enhance in resistivity below 600 °C is more challenging which is respond by motional enthalpy of polaronic conduction. Figure 5.31 shows the Arrhenius plots of the electrical conductivity of $Sr_{1.95}Sm_{0.05}NiMoO_{6-\delta}$ (SSNM05) in H_2 atmosphere was measured during the cooling process. The electrical conductivity in H_2 atmosphere is highly applicable as anode for SOFC application. The observed value of electrical conductivity depends on the reduced state of the sample.

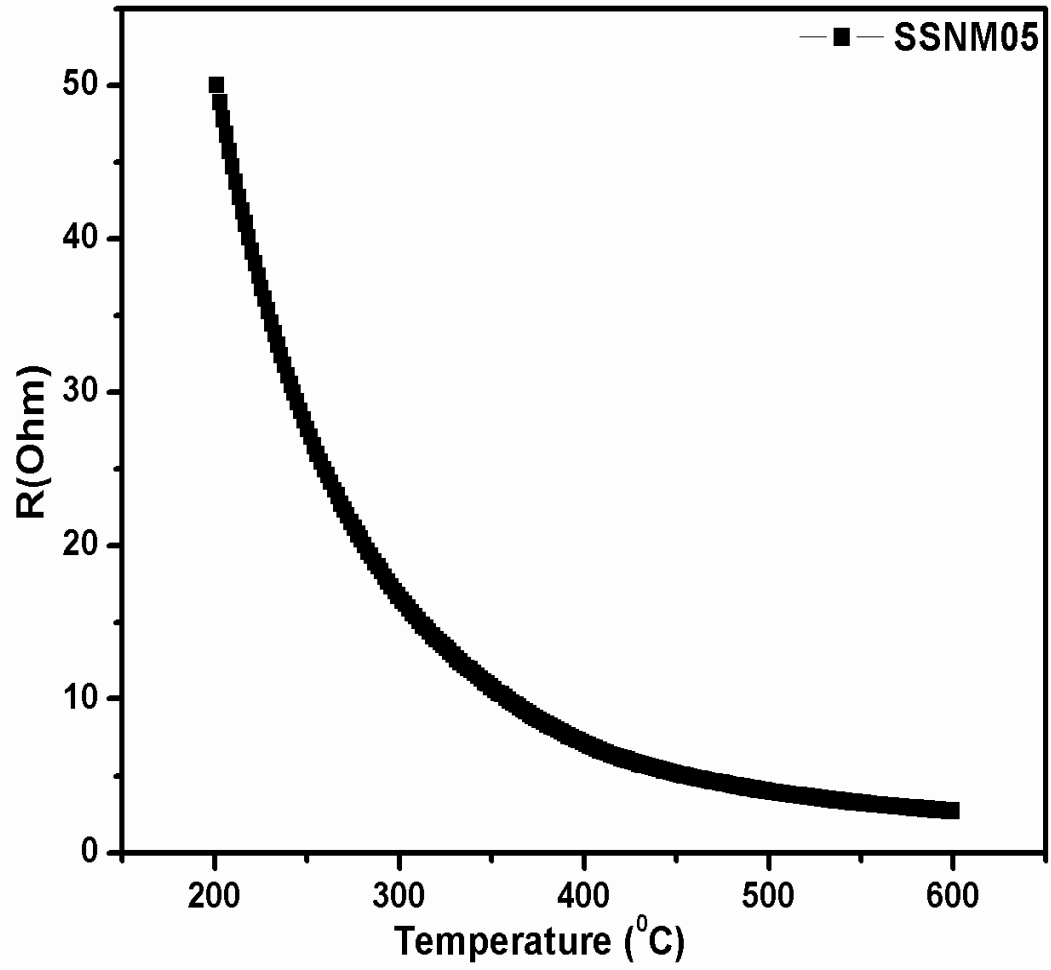

Fig.5.30. *The plots of Resistances as a function of temperature for the sample SSNM05 in H_2 atmosphere.*

Figure 5.31 shows the electrical conductivity of SSNM05 in air and H_2 atmosphere plotted in Arrhenius fashion. From XPS result, it was found that the substitution of rare earth Sm^{3+} at Sr^{2+} site in leads to the reduction of Mo^{6+} to Mo^{5+} ions, which may generates electronic charge carriers and results good electronic conduction. Zhang et al. [2011] reported that the electronic conduction in double perovskite attributes to electron hopping between oxygen ions and mixed valence charge Mo^{5+}/Mo^{6+} cations. The oxygen vacancies formation reduces Mo^{6+} in to Mo^{5+} which contributes to the formation of Mo^{5+} and small polarons and support in excellent mixed electronic-ionic conduction [Huanng et al. (2006) and Ullmann et al. (2000)]. The activation energy (E_a) of SSNM05 sample is calculated from Arrhenius plots and found to be 0.87 eV and 0.32 eV in air and H_2, respectively. It was observed that the value of E_a in reducing atmosphere is lower to that of its value in air.

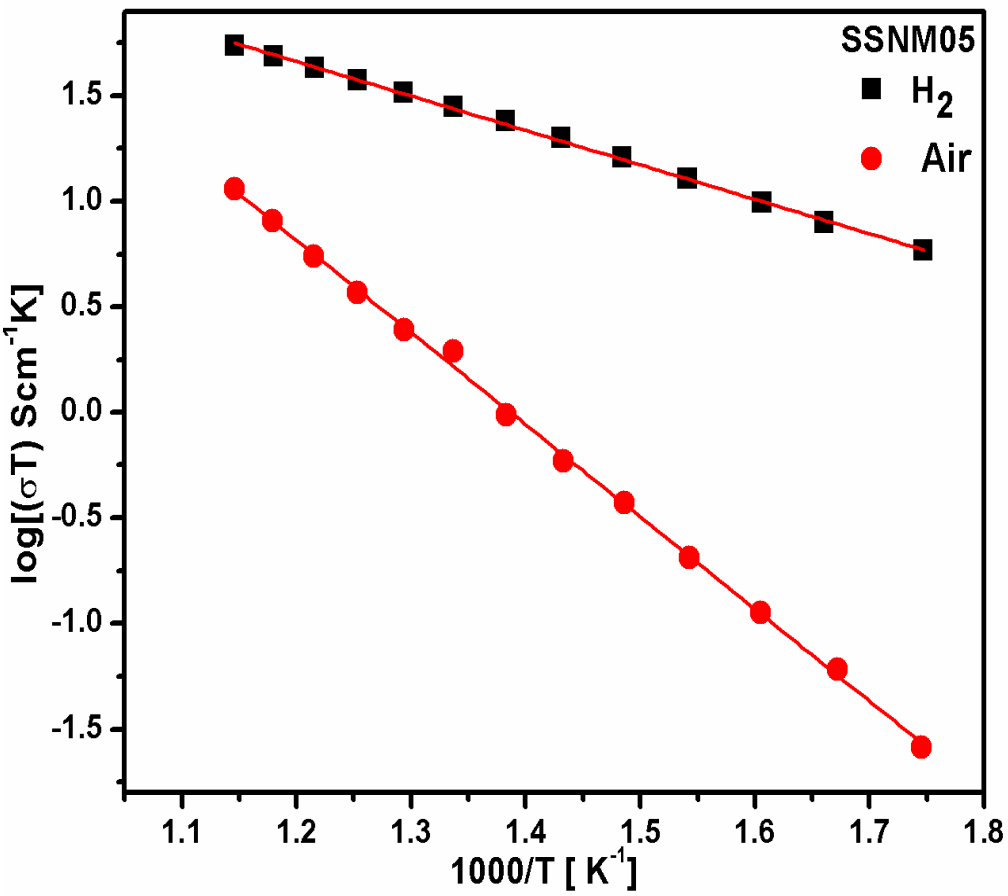

Fig.5.31. *Arrhenius plots of conductivity for the SSNM05 sample in H_2 and air atmosphere.*

The conductivity of SSNM05 sample increases in reducing atmosphere. The increase of conductivity in H_2 atmosphere exhibits polaronic conduction in entire temperature range [Huang et al. (2006)]. Sm^{3+} doping on Sr^{2+} site in Sr_2NiMoO_6 system can be explained from defect Eqns (5.15). During reduction process, oxygen vacancies are created due to reduction of M^{6+} to Mo^{5+} for electronic charge compensation and can be described by following eq^n.

$$2Mo_{Mo}^{\times} + O_O^{\times} \rightarrow 2Mo'_{Mo} + V_o^{\bullet\bullet} + \frac{1}{2}O_2(g) \uparrow \quad (5.16)$$

where electronic charge $Mo'_{Mo}$are generated with substitution Mo^{5+} to Mo^{6+}. The electro-neutrality condition will be maintained by following eq^n.

$$[Mo'_{Mo}] \rightarrow [Sm_{Sr}^{\bullet}] + 2[V_o^{\bullet\bullet}] \quad (5.17)$$

The donor Sm^{3+} substitution at Sr^{2+}site is charge balanced by the increase of electronic charge Mo'_{Mo} concentration and/or decrease of oxygen vacancy concentration. Eq^n.(5.17) gives proper description to enhance the electronic conductivity and decrease the ionic conductivity.

5.4.2 Conclusions

Double perovskite system $Sr_{2-x}Sm_xNiMoO_{6-\delta}$ (SSNM) with $0.01 \leq x \leq 0.05$ has been prepared successfully with a minor phase of $SrMoO_4$. The thermal study shows the two step loss of oxygen around 500 ^{0}C and 850 ^{0}C temperatures. Micro-structural studies revealed that for 3% doping of samarium, the grain has bigger size than that of the other samples but for the composition having 5 mole % samarium, grain has smaller size. The XPS result confirms the presence of mixed valence state of Mo^{6+} to Mo^{5+}. The doping of samarium increases the electrical conductivity of the studied system due to the production of more electronic charge carriers. The sample SSNM05 has highest conductivity with lowest activation energy of 0.88 eV in air and it gets further low activation energy of value 0.32 eV in H_2. Composition SSNM05 has better electronic conductivity and hence it may act as a potential anode candidate in solid oxide fuel cells.